Multi-Objective CubeSat Constellation Optimization for Space Situational Awareness

AE8900 MS Special Problems Report
Space Systems Design Lab (SSDL)
Guggenheim School of Aerospace Engineering
Georgia Institute of Technology
Atlanta, GA

Author:
Adam C. Snow

Advisor:
Marcus J. Holzinger

December 11, 2015

Multi-Objective CubeSat Constellation Optimization for Space Situational Awareness

Adam C. Snow*

The proliferation of on-orbit debris has motivated much of the recent space situational awareness (SSA) missions and related research. Space-based missions are typically carried out by large spacecraft, yet the emerging and improving technology for CubeSat class satellites offers a potential new platform for SSA. This paper presents the graduate Special Problem effort to develop explore the optimization of a CubeSat constellation for SSA. This optimization approach considers two objectives: to maximize the number of daily unique detections while minimizing the lifecycle cost of a constellation. The epsilon constraint method is used to develop the Pareto Frontier with a genetic algorithm as the single-objective optimizer. This work was prepared as part of a larger effort for the Journal of Spacecraft and Rockets, and the supporting material is included.

Nomenclature

a	= Semi-major axis
$\hat{\mathbf{a}}$	= Hyperplane defined by a normal vector
$\mathbf{d}$	= Spacecraft parameters
$\mathbf{e}$	= Environmental parameters
i	= Inclination
l	= Focal length
m	= Number of pixels covered by space object streak
n_i	= Number of image frames per
m_v	= Limiting magnitude integration period
$\mathbf{o}$	= Observer inertial location
$\dot{\mathbf{o}}$	= Observer inertial velocity
$\mathbf{p}$	= Space object parameters
$\hat{\mathbf{p}}$	= Observer boresight vector
q	= Per pixel count rate
$\mathbf{r}$	= RSO intertial location
$\dot{\mathbf{r}}$	= RSO inertial velocity
$\hat{\mathbf{s}}$	= Unit vector in the direction of the sun
t	= Time
$\mathbf{x}$	= Inertial position and velocity state
z	= Number of pixels used to determine background noise
$\mathbf{z}$	= Spacecraft states
$\dot{\mathbf{z}}$	= Spacecraft and attitude dynamics
B	= Wright Model learning curve coefficient
C	= Cost function
D	= Aperture diameter
F	= Lines of flight software code
$\tilde{F}$	= Fraction of all RSOs detected by a constellation for all RSO parameters and environmental conditions
G	= Lines of ground station code
N	= Number of observer satellites
P	= Number of orbital planes
$\mathbf{R}$	= Right-handed rotation matrix
$\mathbf{R}_e$	= Radius of the Earth
S	= Number of satellites in a Walker

*Graduate Student, School of Aerospace Engineering, and AIAA Student Member.

constellation

T = Set of time values

X = Subsystem mass

FOV = Field of view of an EOS sensor

FTT = Cost of a full time technician

FTE = Cost of a full time engineer

IFOV = Instantaneous field of view

NRE = Cost of a non-recurring expense

QE = Quantum efficiency

SNR = Signal to noise ratio

TFU = Cost of a theoretical first unit

$\mathcal{D}$ = Geometrically Detectable Subspace

$\mathcal{E}$ = The set of environmental parameters

$\mathcal{N}$ = Inertial frame

$\mathcal{P}$ = The set of space object parameters

$\mathcal{O}$ = EOS boresight frame

$\mathcal{U}$ = Uniform distribution

$\mathcal{X}$ = The set of full object states

$\mathcal{Z}$ = The set of admissible decision parameters

$\mathbb{N}$ = The set of natural numbers

$\mathbb{R}$ = The set of real numbers

α = Coefficient of commercial development

$\dot{\eta}$ = Apparent angular rate

θ = Angle between inertial location vector and Earth-tangent line of sight

$\boldsymbol{\theta}_a^b$ = Rotation between inertial frames a and b

$\boldsymbol{\kappa}$ = Constraint Equation

ν = F-number

$\boldsymbol{\rho}$ = Distance between two inertial points

σ_r = EOS read noise

τ = Transmittance

ϕ = Solar phase angle

$\boldsymbol{\omega}_a^b$ = Angular rate of b in frame a

E = Epsilon constraint

Φ = Spectral excitance

Ω = Total set of geometrically detectable states and times for an entire constellation

$\tilde{\Omega}$ = Total set of geometrically detectable states and times for an entire constellation for all RSO parameters and environmental conditions

Subscripts

$_{\text{alg}}$ = Detection algorithm

$_{\text{bkg}}$ = Background

$_C$ = Image cadence

$_d$ = Spacecraft parameters d

$_h$ = Horizontal

$_i$ = i^{th} observing satellite

$_I$ = EOS integration

$_j$ = j^{th} space object

$_k$ = k^{th} satellite subsystem

$_N$ = Number of satellites

$_p$ = Image processing; pixel

$_o$ = Initial value

$_t$ = Transfer

$_v$ = Vertical

$_z$ = Decision variables

$_{RSO}$ = Resident Space object

$_{\mathcal{L}}$ = Line of sight

$_{\mathcal{F}}$ = Field of view

$_{\mathcal{I}}$ = Illumination

$_{\parallel}$ = Tangent to the Earth

Superscripts

^{T} = Matrix transpose

$^{\mathcal{O}_i}$ = Observer reference frame

^{r} = Dimension of $\mathcal{P}$

^{v} = Dimension of ε

$^+$ = Positive real numbers

I. Introduction

Space Situational Awareness (SSA) is a growing concern for both government and private sectors, as it threatens both national security and commercial interests. The quantity of Resident Space Objects (RSOs) is growing rapidly due to continual satellite launch, in-space collisions, and anti-satellite activity. The majority of data on RSOs comes from the US Department of Defense Joint Space Operations Center (JSpOC). This data is gathered through the Space Surveillance Network (SSN) that JSpOC tasks with the observation and tracking of RSOs. There are currently in excess of 21,000 LEO objects with diameters above 10 cm [3] in the JSpOC space object catalog(SOC).

The threat of RSOs on space assets continues to grow. Though object removal is the eventual solution, the first step is significantly increased awareness of the space environment. It is estimated that there are hundreds of thousands of RSOs that are difficult to detect and track due to their small size. Given the significant gap in our current understanding, it is critical for cost effective means of SSA be developed and deployed. This Special Problem effort was prepared as part of a pending publication in the Journal of Spacecraft and Rockets. This journal artical presents a constellation of CubeSats as a viable means for SSA both in terms of performance and cost effectiveness.

The journal article had three primary contributions. First it proposed a formal definition for SSA performance given the LEO space environment and defined a preferred CONOPS for a LEO observer spacecraft. Second it developed a sequential optimization approach to the CubeSat constellation design problem. A complete system optimization effort would be computationally intractable. Instead, this paper presents first a qualitative optimization of an individual spacecraft followed by a computational constellation optimization. Finally, the journal paper presented a multi objective constellation optimization problem. This final contribution is the main contents of this Special Problem effort.

The optimization problem begins by describing the sequential optimization approach employed. The contributions in the journal article can be found in §V. This optimization effort two objective functions and generates the Pareto frontier of trade offs between the objective of maximizing daily unique detections of the constellation and minimizing the lifecycle cost. The optimization problem used a fixed-step two body propagator of the known RSOs in the Space Object Catalog along with a set of observer spacecraft in a Walker-Delta configuration. Using the photometric relationships developed by Ryan Coder, the optimizer is able to determine the detection capability of a given constellation. The lifecycle cost of a constellation design is determined through the use of parametric cost estimating relationships. The Pareto Frontier is developed through the use of the Epsilon constraint method to simplify the mutli-objective optimization problem into a series of single objective optimization problems. A genetic algorithm is used as the single objective optimizer as its stochastic nature is well suited for the non-differentiable and discontinuous nature of the objective space. The effort shows that a constellation of CubeSats represents a powerful yet cost effective method for space situational awareness.

II. Constellation Design

The performance of many space missions is enhanced through the utilization of a constellation architecture. For SSA missions, constellations are particularly valuable for maximizing the quantity of detections from a space based platform. By deploying multiple sensors that are distributed throughout the orbit environment, a constellation based SSA mission can significantly increase detection performance. The recent developments in small satellite systems have given rise to several other benefits in constellation design as well [43]. First, a constellation is a fractionated and disaggregated system that is resilient to single satellite failure. Second, constellations are highly scalable in that they can be incrementally deployed, providing financial and operational flexibility for mission planners. Finally, this incremental deployment results in a much higher technology refreshment rate than larger satellite missions. With a shorter life time and scalable architecture, sequential satellite deployments can take advantage of incremental technology improvements, leading to more adaptive system architectures. These benefits make the utilization of a constellation architecture highly attractive in the design of a space situational awareness campaign.

The optimization problem articulated in Problem 1 describes the performance optimization of a constellation across all relevant decision variables. The objective function $\tilde{F}_N(\mathbf{z}, T)$ depends on the number of spacecraft N, the inertial observer states $\mathbf{x}_{o,i}$, orientation states $(\boldsymbol{\theta}_{\mathcal{N}}^{\mathcal{O}_i}(t), \boldsymbol{\omega}_{\mathcal{N}}^{\mathcal{O}_i}(t))$, and spacecraft design parameters $\mathbf{d}_i \ \forall i = 1, \ldots, N$. As described in §VI.H, this optimization problem is analytically clear, but computationally intractable. To enable a computationally manageable yet still meaningful optimization effort, several decision variables are qualitatively optimized and are treated as constraints. Particularly, §VI.G describes the attitude profile of each satellite in the

constellation to individually maximize detections by tracking the regions of largest spatial density. Additionally, §VII describes the relevant spacecraft parameters $\mathbf{d}_i$ so as to maximize the optical properties of a COTS payload suitable for CubeSat missions. Once these decision parameters are constrained, the remaining optimization problem involves a more traditional constellation optimization problem dependent on only N and $\mathbf{x}_{o,i}$. This simplified version of Eqn.(44) is combined with an objective function for lifecycle cost to present a full MOO problem. The full list of parameters are listed in Table 6, including the remaining variables to be optimized.

A. Performance Simulation

A thorough discussion of the conditions for RSO detection and CubeSat constellation SSA mission CONOPS is presented in §VI. To quantify the outcome of these analytical models on a given constellation architecture, a detailed SSA mission simulator is developed. This simulator leverages much of the work done at Georgia Tech in the realm of space situational awareness and propagation modeling [60], and enables numerical evaluation of Eqn. (44).

The simulation begins by generating a fixed set of N surveillance spacecraft that are defined with an initial state $\mathbf{x}_{o,i,0}$. The attitude trajectory for each spacecraft is described in §VI.G over the simulation time period , $t \in T$. This trajectory assigns three pointing targets for the spacecraft. The rings above the northern and southern poles defined by 900km altitude, sun synchronous orbits are chosen as the pointing target when the spacecraft is above/below the ecliptic plane. A specific location on this ring is targeted based on the best solar phase angle. As the spacecraft is crossing the ecliptic plane, the pointing target is at GEO altitude in the radial direction of the satellite position. These pointing targets are achieved by a simple first order filter with a time constant representative of a CubeSat ADCS subsystem.

Each spacecraft also is assigned the same EOS payload parameters selected in §VII and are shown again in Table 6. These parameters correspond to the Photonis Nocturn XL imager and the Kowa LM60JS5MA lens, which is the combination with the highest limiting magnitude which implies high detection capability. The dynamics $\mathbf{f}_z(\mathbf{z}, t)$ for all spacecraft and objects are given by the equations of motion of the two-body problem using a fixed time step integrator. Fixed step integration is chosen to simplify the coordination of the simulation of the each of the RSO and observer orbits.

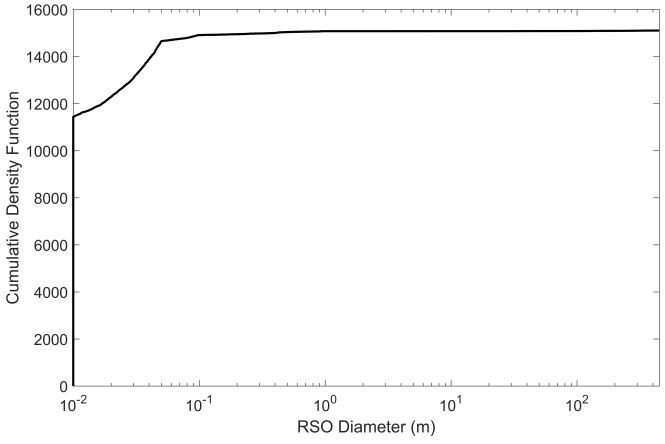

Figure 1. Distribution of object diameter used in the simulation

Each RSO is assigned a random initial set of properties $\mathbf{p}_j$ that give the orbit and optical characteristics for the

[a]For computational reasons, this simulation only takes an image once each 60 seconds, but an operational cadance could be 1-2 seconds.

Table 1. Decision variables, z

Parameter	Symbol	Units	Value
CONOPS Variables:			
Translational States	$\left(\mathbf{o}_i^T(t),\ \dot{\mathbf{o}}_i^T(t)\right)$	—	function of (N, P, a, i)
Rotational States	$\left(\boldsymbol{\theta}_{\mathcal{N}}^{\mathcal{O}_i}(t), \boldsymbol{\omega}_{\mathcal{N}}^{\mathcal{O}_i}(t)\right)$	—	function of (N, P, a, i)
Payload Parameters, $\mathbf{d}_i$:			
Signal to Noise Ratio	SNR_{alg}	—	4
Pixels occupied by RSO	$m_{ij,0}$	pixels	1
Focal length	l	mm	60.0
F-number	ν	—	0.80
Aperture diameter	D	mm	75.0
Horizontal FOV	FOV_h	deg	14.23
Vertical FOV	FOV_v	deg	11.38
Pixel size	p	μm	9.7
Sensor resolution	$n_{p,h} \times n_{p,v}$	pixels	1280×1024
Quantum Efficiency	QE	—	0.60
Optical transmittance	τ_{opt}	—	0.9
Dark current per pixel	$q_{\text{p,dark}}$	e/pixel/s	0.5
Cadence Time[a]	t_C	sec	60
Integration Time	t_I	ms	33
Environmental Parameters, $\mathbf{e}_{ij}$:			
Background radiant intensity	$q_{\text{p,bkg}}$	m_v/as^2	0.0364
Spectral excitement of a magnitude 0 object	Φ_0	photons/s/m^2	5.6×10^{10}
Relative angular rate	$\dot{\eta}_{ij}$	rad/s	function of (N, P, a, i)
Atmospheric transmittance	τ_{atm}	—	1
Constellation Parameters:			
Number of Satellites	N	$\mathbb{N}$	To be optimized
Number of Planes	P	$\mathbb{N}$	To be optimized
Semi-Major Axis	a	km	To be optimized
Inclination	i	$^\circ$	To be optimized

given object. For this simulation the RSO properties include the initial state and the size. The JSpOC SOC is used as an a-priori distribution of RSOs. The PDF for the RSOs from §VI is defined as a uniform PDF over the 15,106 items in this SOC. Each of the simulated RSOs is randomly assumed to be one of the 15,106 items from the SOC. The initial state $\mathbf{x}_{j,0}$ for each of the RSOs is then given by converting the TLE corresponding to the j^{th} SOC item into a cartesian position and velocity. The diameter of each RSO is probabilistically assigned based on an estimated RSO population [69]. The CDF of this distribution is shown in Figure 1. Given the approximation of the space environment using the PDF of object diameters in the SOC, a majority of the objects are set at a user defined 1 cm minimum with relatively few large objects. The SOC is only a partial representation of the true space environment, but is useful as an approximation for this analysis. Thus, while the RSO distribution is uniform over the SOC, the probabilistic RSO size assignment directly impacts the probability of detection through Eqn. (32). As these sizes are randomly assigned

at the beginning of each simulation, a Monte Carlo approach is necessary to evaluate performance.

To numerically determine $\tilde{F}_N(\mathbf{z}, T)$, the geometrically detectable region $\mathcal{D}_i$ must first be computed for each time instant. The simulator propagates each object from its initial state in 60 second time steps for a total duration of 24 hours. As such the operational cadence for the satellites is taken to be 60 seconds, the integration time is set to 0.5 seconds as in §VII. After each propagation step, $\mathcal{D}_i$ is computed by applying each of the constraints defined by $\kappa_{i,\mathcal{L}}$, $\boldsymbol{\kappa}_{i,\mathcal{F}}$, and $\kappa_{\mathcal{I}}$. These constraints fully define $\mathcal{D}_i$ for each observer with respect to the SOC used in the simulation. For each observer i, each RSO in $\mathcal{D}_i$ for that observer is assigned a probability of detection via Eqn. (32). Probability of detection is based on a minimum detectable SNR_{alg} of 4 as given in Table 6. For simplicity, this simulation only considers an object detectable if $p_{d,i}(t_I; \cdot) \geq 0.99$. An example of the results from a single 24 hour period of this simulation with a single observer is shown in Figure 2.

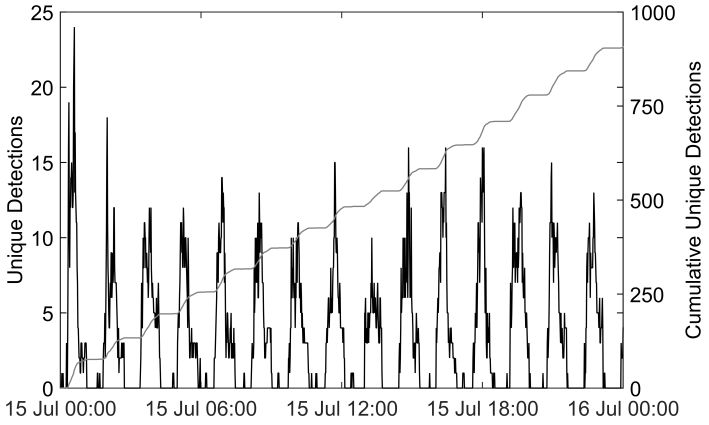

Figure 2. Unique detections. Single Spacecraft, 500 km, 60° inclination

The simulations shown in the remaining section of the paper use 24 hours as the time period for the optimization and analysis. This duration is sufficiently long enough for the LEO observers to complete roughly 15 orbits, which is enough to establish the cyclical detection trends that can be seen in Figure 2. Furthermore, while longer observation periods may allow additional trends to be observed, this is a highly computationally intensive problem and it is computationally prohibitive to simulate for many days without increasing the time step. In addition, the 60 second cadence is deemed sufficient to capture the general detectability trends. It is clear that with a shorter cadence, such as given in Figure 3, the expected total number of detections as well as the number of unique detections will increase. But since for the work shown in this paper it is more important to show the general trends in detectability and since the computational requirements for short cadence simulation is high, the 60 second cadence is justified. Lastly, due to the stochastic nature of RSO size assignment, each of the optimization analyses averages over 10 simulations of the constellation's detection performance.

B. Objective Space

This detailed performance simulation can be utilized in an optimization algorithm to maximize the performance of a constellation of space sensors. In this optimization effort, two performance parameters are used to evaluate mission design. The first objective is to maximize the detection capability of a constellation $\tilde{F}_N(\mathbf{z}, T)$, and the second objective is to minimize lifecycle cost $C(N, \mathbf{d}_i)$. These two objectives are inversely proportional, making the definition of an optimal solution unclear. Many previous constellation optimization efforts have utilized similar objective functions to establish a set of Pareto-optimal solutions [46]. These algorithms develop a Pareto frontier of design points that represent tradeoffs between mission performance and mission cost objectives. More formally, the optimization algorithm

employed here can be described as:

$$
\begin{aligned}
\min_{N,P,a,i} \; & J_1\big(N, \mathbf{z}(N,P,a,i), T\big) = -\tilde{F}_N\big(\mathbf{z}(N,P,a,i), T\big) \\
& J_2\big(N, \mathbf{z}(N,P,a,i), T\big) = C(N, \mathbf{d}_i) \\
& \text{subject to: } \dot{\mathbf{z}} = \mathbf{f}_z\big(\mathbf{z}(N,P,a,i), t\big), t \in T \\
& \mathbf{z}(N,P,a,i) \in \big(\mathcal{X} \times \mathrm{SO}(3) \times \mathbb{R}^3 \times \mathcal{P}\big) \times N \\
& N, P \in \mathbb{N} \\
& \begin{bmatrix} 1 \\ 1 \\ 6578 \text{ km} \\ 0^\circ \end{bmatrix} \leq \begin{bmatrix} N \\ P \\ a \\ i \end{bmatrix} \leq \begin{bmatrix} 36 \\ 36 \\ 7678 \text{ km} \\ 100^\circ \end{bmatrix}
\end{aligned}
$$

The first objective function is a measure of the constellation's detection performance introduced in section §VI.H, and is a function of the constellation configuration. As the optimization methodology seeks to minimize both objective functions, the negative value of SOC coverage is considered, and thus a maximum absolute value of unique detections is pursued. There are several ways to configure the satellite constellation, yet the Walker delta pattern [70] has been commonly used for initial constellation design, as it evenly distributes the satellites throughout the orbit environment. A Walker delta constellation is characterized by N satellites distributed across P planes with $S = N/P \in \mathbb{N}$ satellites per plane. All satellites share the same semi-major axis a, eccentricity, and inclination i but are phased in terms of argument of periapse and right ascension of ascending node. The ascending nodes of the P orbital planes are distributed evenly at intervals of $360/P$. Similarly the S satellites in each orbital plane are distributed evenly at intervals of $360/S$. Finally, the phase difference angle $\Delta\psi$ represents the difference in argument of periapse between adjacent planes. This phase difference angle must be an integer multiple of $360/N$. The Walker delta configuration ensures that all satellites are evenly distributed throughout the orbit environment. This analysis only considers constellations of up to 50 satellites in 50 orbital planes with circular orbits, orbital altitudes between 500 and 1300 km, and inclinations ranging from equatorial to sun-synchronous configurations. These side constraints are chosen to reflect constellation configurations common to the CubeSat platform.

C. Lifecycle Cost Estimation

After considering the detection performance of a constellation of satellites, the lifecycle cost of deploying these satellites must be considered. In contrast to the performance simulation, which is evaluated through numerical simulation, the lifecycle cost is evaluated much more analytically. The total cost $C(N, \mathbf{d}_i)$ is given by,

$$
C(N, \mathbf{d}_i) = C_{\text{DDT\&E}}(\mathbf{d}_i) + C_{\text{Prod}}(N, \mathbf{d}_i) + C_{\text{Launch}}(N, \mathbf{d}_i) + C_{\text{O\&S}}(N, \mathbf{d}_i) + C_{\text{Wraps}}(N, \mathbf{d}_i) \tag{1}
$$

where $C_{\text{DDT\&E}}(\mathbf{d}_i)$ is the cost of the design, development, testing, and evaluation (DDT&E) of a constellation of satellites with parameters $\mathbf{d}_i$, $C_{\text{Prod}}(N, \mathbf{d}_i)$ is the production cost of all N satellites with parameters $\mathbf{d}_i$, $C_{\text{Launch}}(N, \mathbf{d}_i)$ is the cost to deploy all satellites in the constellation, and $C_{\text{O\&S}}(N, \mathbf{d}_i)$ is the cost of operations and support of the satellites once on orbit. $C_{\text{Wraps}}(N, \mathbf{d}_i)$ captures the program level and overhead costs associated with the mission. Each of these costs can be estimated analytically through the use of parametric cost estimating relationships (CERs) from one of several available cost estimation models [71]. CERs are derived from historical spacecraft missions, and seek to establish an approximate relationship between specific spacecraft parameters and cost. These approximations are highly dependent on the historical spacecraft considered and are only fit within specified ranges.

Due to recent advancements in small satellite technology, all of the publicly available cost models are outside of relevant ranges [72]. The success of the CubeSat platform has been in part to the economic advantages of lower hardware costs and development requirements, enabling a wide variety of mission architectures. Since these changes have been relatively recent, parametric models have not had sufficient time to incorporate historical data to form new parametric relationships. Despite these limitations, it is useful to employ these parametric models as they provide a relative scale by which to compare constellation designs. For this effort, the Small Satellite Cost Model (SSCM) developed by the Aerospace Corporation is used as its relevant range is most similar to the nanosatellite constellation considered here [73]. Portions of several other historical models are employed to account for the limitations in the SSCM alone, particularly the sizing cost distribution rankings developed by Microcosm [43].

As the proposed CubeSat constellation lacks definition of the particular business and programmatic environment, several assumptions must be made. As this constellation architecture is further developed, these assumptions must be refined to be relevant to business decisions. However, these assumptions suffice for the purpose of evaluating conceptual constellation performance. The high level costing assumptions are given as:

1. The proposed CubeSat constellation is developed, produced, and operated in a commercial environment, accounting for all relevant business expenses.
2. All constellation sizes spend two years in development, six months in dedicated production, and one year of operation. All constellations are launched and operated at once.
3. Each spacecraft in the proposed constellation have identical parameters $\mathbf{d}$ where $\mathbf{d}_i = \mathbf{d}$ for all $i = 1, ..., N$.

The first step in the cost estimation process is to develop the spacecraft parameters $\mathbf{d}$ that inform the CERs. The CERs used in the SSCM are based on subsystem mass. For this analysis, historical mass distributions are used to size each of the spacecraft subsystem [74] along with an estimate for payload mass from §VII.

Table 2. Spacecraft Mass Distributions [74]

Subsystem	Percent Mass	σ
Payload	26.7%	7.5%
Structure	21.7%	5.3%
Thermal	3.4%	3.0%
Power	27.9%	6.6%
C&DH	7.5%	5.5%
ADCS	8.0%	4.7%
Comm	4.8%	1.0%

Next, these mass estimates can be used to estimate costs using parametric models. The SSCM utilizes a protoflight approach, where the fabrication of the first flight unit is included in the development process [73]. This first flight unit is referred to as the theoretical first unit (TFU) and is used as a starting point for estimating C_{Prod}. Therefore, the CERs given in the SSCM provide the cost of $C_{\text{DDT\&E}} + C_{\text{TFU}}$. In Eqns. (2)-(7), the independent variable is subsystem mass X in kilograms. The cost of the payload is estimated from the sum of other subsystem costs.

$$C_{\text{Comm}}(\mathbf{d}) = \alpha(357 + 40.6 \cdot X_{\text{Comm}}^{1.35}) \tag{2}$$

$$C_{\text{Struct}}(\mathbf{d}) = \alpha(299 + 14.2 \cdot X_{\text{Struct}} \cdot \ln(X_{\text{Struct}})) \tag{3}$$

$$C_{\text{Therm}}(\mathbf{d}) = \alpha(246 + 4.2 \cdot X_{\text{Therm}}^{2}) \tag{4}$$

$$C_{\text{Power}}(\mathbf{d}) = \alpha(-923 + 396 \cdot X_{\text{Power}}^{0.72}) \tag{5}$$

$$C_{\text{TT\&C}}(\mathbf{d}) = \alpha(484 + 55 \cdot X_{\text{TT\&C}}^{1.35}) \tag{6}$$

$$C_{\text{ADCS}}(\mathbf{d}) = \alpha(1358 + 8.58 \cdot X_{\text{ADCS}}^{2}) \tag{7}$$

$$\begin{aligned} C_{\text{Bus}}(\mathbf{d}) = C_{\text{Comm}}(\mathbf{d}) + C_{\text{Struct}}(\mathbf{d}) + C_{\text{Therm}}(\mathbf{d}) \\ + C_{\text{Power}}(\mathbf{d}) + C_{\text{TT\&C}}(\mathbf{d}) + C_{\text{ADCS}}(\mathbf{d}) \end{aligned} \tag{8}$$

$$C_{\text{Payload}}(\mathbf{d}) = 0.4 \cdot C_{\text{Bus}}(\mathbf{d}) \tag{9}$$

The cost estimates from the SSCM are in FY00$K which are inflated to FY15$K dollars [73]. Additionally, a coefficient of $\alpha = 0.8$ is applied to account for the assumption of commercial development based on historical programs [43]. As these cost estimates include both non-recurring expenses and recurring expenses, the nonrecurring $C_{\text{DDT\&E}}$ is determined summing the non-recurring portion of costs for each k subsystems [43].

$$C_{\text{DDT\&E}}(\mathbf{d}) = \sum \text{NRE}_k \cdot C_k(\mathbf{d}) \tag{10}$$

with NRE_k given by the historical distributions shown in Table 3.

Table 3. Non-Recurring Expenses

Subsystem	Non-Recurring Percentage
Payload	60%
Structure	70%
Thermal	50%
Power	62%
C&DH	71%
ADCS	37%
Comm	71%

At this point a slight deviation in the SSCM is employed to account for the CubSat design paradigm. TFU cost can be considered to broadly include hardware costs and labor costs. Due to the standardization of CubeSat components, a survey of COTS components can be conducted to develop a bottoms-up estimate for the hardware costs for the TFU. The labor costs for TFU can be estimated as the recurring portion of C_{Wraps} described later, particularly $C_{\text{IA\&T}}$, C_{PMSE}, and C_{LOOS} [43]. To account for uncertainty, a 20% contingency is included with each subsystem estimate in addition to a 20% system level margin [43]. A summary of the survey results employed here is shown in Table 4.

As the constellation increases in size, the production cost of each incremental unit decreases due to higher efficiency. To account for this, the Wright Model learning curve shown in Eqn. (11) is employed [43].

$$C_{\text{Prod}} = \text{TFU} \cdot N^{B} \tag{11}$$

Where B is the learning curve coefficient applied, 0.95 here. This low level of learning is based on the predominant use of COTS components. The development and production costs are wrapped in program level costs associated with the management and overhead for the project prior to launch, C_{Wraps}. These program level costs include Program Management and Systems Engineering (PMSE), Integration, Assembly, & Testing (IA&T), Ground Support Equipment (GSE), and Launch & Orbital Operations Support (LOOS). The CERs for C_{Wraps} are shown in Eqns. (12)-(15).

Table 4. Spacecraft Hardware Costs

Subsystem	Component	Manufacturer	Cost Estimate
Payload	Nocturn	Photonis	\$3,904
	Lens	Kowa	\$1,800
	Frame Grabber	Pleora	\$1,495
Structure	6U Structure	Pumpkin	\$14,500
EPS	Power Management	Clyde Space	\$10,550
	30 Whr Battery	Clyde Space	\$3,850
	6U Solar Array (x2)	Clyde Space	\$14,300
	3U Solar Array (x2)	Clyde Space	\$6,050
C&DH	Tyvak Intrepid	Tyvak	\$5,500
ADCS	Control Module	ISIS	\$4,650
	Sun Sensors (x4)	ISIS	\$2,500
Thermal	MLI	McMaster Carr	\$2,000
Telecom	S-band Transmitter	ISIS	\$9,350
	S-band Antenna	ISIS	\$5,050
	Tyvak UHF	Tyvak	\$3,000
	UHF Antenna	ISIS	\$4,950
	System Margin		20%
	Total Hardware		\$166,318

$$C_{\text{IA\&T}} = 0.139 \cdot (C_{\text{DDT\&E}} + C_{\text{Prod}}) \tag{12}$$

$$C_{\text{PMSE}} = 0.229 \cdot (C_{\text{DDT\&E}} + C_{\text{Prod}}) \tag{13}$$

$$C_{\text{GSE}} = 0.066 \cdot (C_{\text{DDT\&E}} + C_{\text{Prod}}) \tag{14}$$

$$C_{\text{LOOS}} = 0.061 \cdot (C_{\text{DDT\&E}} + C_{\text{Prod}}) \tag{15}$$

$$C_{\text{Wraps}} = C_{\text{IA\&T}} + C_{\text{PMSE}} + C_{\text{GSE}} + C_{\text{LOOS}} \tag{16}$$

In addition to having standardized components, CubeSat vehicles also benefit from standardized launch costs. Launch costs are estimated at $C_{\text{Launch}} = \$546,500$ per unit based on secondary payload manifesting prices for a 6U CubeSat along with the price of a deployment device

The final cost component in lifecycle cost deals with the operation and maintenance of the spacecraft once on orbit, C_{Ops}. These costs are primarily driven by the amount of flight and ground software that need to be maintained during the mission lifetime. These values scale with the number of satellites, as larger constellations require more effort to operate and maintain. The operational lifetime is considered to be a single year. In general, C_{Ops} can be considered in the three distinct categories of mission operations labor, hardware and facilities, and program management.

$$C_{\text{Labor}} = N \cdot \left(\frac{F}{16} + \frac{G}{28}\right) \cdot (\text{FTE+FTT}) \tag{17}$$

$$C_{\text{Ops}} = C_{\text{Labor}} + C_{\text{Facilities}} + C_{\text{PMSE, Ops}} \tag{18}$$

Estimates for the flight software and ground software required to operate each satellite can be generated in terms of thousand lines of code (KLOC). From historical trends, each satellite requires 7.8 KLOC flight software, F, and

17.0 KLOC for ground software, G [43]. A full time engineer (FTE) can operate and maintain 16 KLOC of flight software or 28 KLOC of ground software per year [43]. Here it is assumed that there is one full time tech (FTT) per FTE with annual rates of $150,000 and $220,000 respectively [43].

$C_{\text{Facilities}}$ involves the hardware maintenance, rental equipment, and office space required through mission operations. Here, this category is simplified to $C_{\text{Facilities}} = 5\% \cdot C_{\text{GSE}} + C_{\text{Lease}}$. The maintenance of GSE hardware is simple 5% of C_{GSE}, and the lease of all office space and ground station facilities is estimated at $250,000. Finally, $C_{\text{PMSE, Ops}} = 0.05 \cdot C_{\text{Labor}} + C_{\text{Facilities}}$ [43].

III. Optimization Methodology and Results

There are several common methods for analyzing MOO problems. The most common methods establish a new objective function of non-domination for evaluating design points. These algorithms create the Pareto frontier by compiling points that are non-dominated with respect to the multiple design objectives, that is, for each design point the aggregate objective function is at least as good as all other design points in one or more objective function axis [75]. Non-domination algorithms such as NGSA-II are very useful as they can comprehensively and clearly define the Pareto frontier; however, as this optimization effort involves lengthy and complex numerical evaluation of design points, a more simple algorithm is considered.

The MOO method employed here is the epsilon constraint method [76]. This method involves a series of sequential optimization algorithms that solve for one of the multiple objective functions while considering all others as equality constraints. The epsilon constraint method requires that the Pareto frontier be monotonic; at a fixed point for one objective function, there is only one point along the other objective functions that are on the Pareto frontier. As only two objective functions are considered here, the epsilon constraint method is quite straightforward to implement. Moreover, the objective functions employed here can be further decoupled by considering the fact that the only design variable shared between the two objective functions is N, the number of satellites in the constellation. A set of 10 optimizations are performed for each $N \in \mathcal{N}$, each time randomly initializing the SOC objects with sizes drawn from the appropriate distribution. The formal definition of the epsilon constraint function is given below.

$$
\begin{aligned}
&\text{for each } E \in \mathcal{N} = \{1, 2, 4, 6, 8, 12, 18, 24, 36\} \subset \mathbb{N} \\
\min_{N,P,a,i} \; & J_1\big(N, \mathbf{z}(N, P, a, i), T\big) = -\tilde{F}_N\big(\mathbf{z}(N, P, a, i), T\big) \\
&\text{subject to: } \dot{\mathbf{z}} = \mathbf{f}_z\big(\mathbf{z}(N, P, a, i), t\big), t \in T \\
&\mathbf{z}(N, P, a, i) \in \big(\mathcal{X} \times \text{SO}(3) \times \mathbb{R}^3 \times \mathcal{P}\big) \times N \\
&N = E \\
&P \in \mathbb{N} \\
&\begin{bmatrix} 1 \\ 6578 \text{ km} \\ 0^\circ \end{bmatrix} \leq \begin{bmatrix} P \\ a \\ i \end{bmatrix} \leq \begin{bmatrix} 36 \\ 7678 \text{ km} \\ 100^\circ \end{bmatrix}
\end{aligned}
$$

As the second objective function $C(N, \mathbf{d}_i)$ is dependent only on the number of satellites, it remains constant for each constrained design point in the epsilon constraint method. The lifecycle cost for each $E \in \mathcal{N}$ is given in Figure 3. Parametric CERs include standard error in their approximations based on historical space missions. To consider the effects of these uncertainty measurements on the entire cost estimate, 10 Monte Carlo runs were performed for each epsilon constraint point, providing statistical performance information. The resulting cost estimate shown here display

costs within 3 sigma.

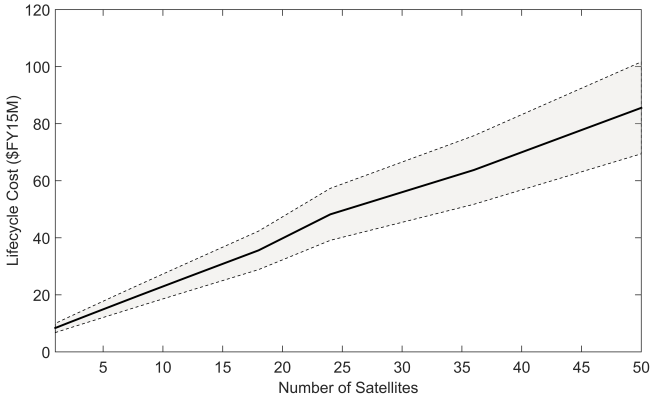

Figure 3. Lifecycle cost objective function $C(N, \mathbf{d})$ vs constellation size N

After considering that the multi-objective problem may be simplified to a series of single objective problems, a single objective optimizer must be selected. Performance simulation based on discrete calculations leads to an objective space that is highly nonlinear and discontinuous. Several optimization algorithms are suited for this optimization problem such as the simulated annealing and iterative mixed-integer methods, but a genetic algorithm is employed for this design problem. Many constellation optimization problems have been addressed using genetic algorithms [46] due to its stochastic nature and ability to freely explore the objective space. Genetic algorithms are metaheuristic algorithms inspired by the reproductive and evolutionary processes found in nature. Since the objective functions used here is nonlinear and non-differentiable, metaheuristic methods are the best suited algorithms for optimization in that they do not rely on knowledge of the objective function. The specific genetic algorithm characteristics employed in this optimization effort are shown in Table 5 and follow the procedures given by D.E. Goldberg [77].

Table 5. Summary of genetic algorithm parameters.

Function	Value
Population Size	20
Generations	15
Elitism Count	2
Selection Method	Roulette
Crossover Fraction	75%
Mutation Fraction	1%
Constraint Evaluation	Exterior Penalty

A. Optimization Results

The performance of the genetic algorithms employed here can be analyzed in terms of convergence and breadth of exploration. To understand convergence behavior, the mean euclidean distance between population members through consecutive generations is analyzed. This performance varies between consecutive optimization iterations within the epsilon constraint method. For an optimization algorithm with $P = 1$, $N = 1$, $a = 6878$ km, and $i = 72°$, convergence is achieved quickly after eight generations as displayed in Figure 4.

One of the most attractive properties to genetic algorithms is their ability to explore the decision space, even

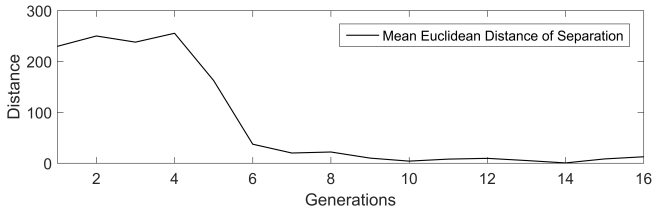

Figure 4. Distance between design points through generations

in later generations. This behavior can be analyzed by considering the range of objective function values through consecutive generations. Figure 5 charts the maximum and minimum values of the objective function among the population. Even though the optimal configuration is part of the first generation, consecutive generations continue to explore the sample space. This stochastic nature reduces the threat of converging to local minima.

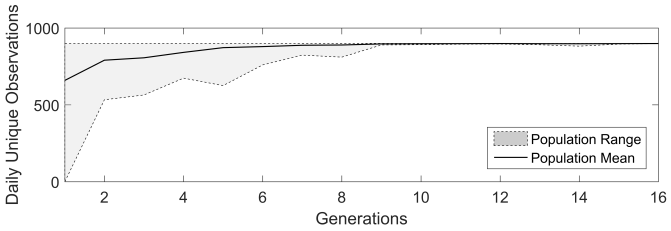

Figure 5. Range of population objective function through generations

In addition to the uncertainty distributions surrounding $C(N, \mathbf{d}_i)$, $\tilde{F}_N(\mathbf{z}, T)$ contains significant uncertainty based on the numerical model applied. In the performance simulation, each object is stochastically assigned a diameter, leading to varying results for the same constellation design across multiple runs. To account for this uncertainty in the development of the final Pareto frontier a series of 10 iterations were performed for each E in the epsilon constraint method, leading to 90 unique optimization problems being performed for $\tilde{F}_N(\mathbf{z}, T)$. Additionally, 90 Monte Carlo runs of $C(N, \mathbf{d}_i)$ were performed at the same E values. The results of these optimization results are displayed in Figure 6 clearly form a Pareto frontier, representing the tradeoffs between the two design objectives. It can be seen that the general shape of the epsilon constraint method is monotonic with repsect to the two objective functions, granting confidence in the use of the epsilon constraint method.

To understand the impact of each of the design variables P, N, a, and i, a univariate sampling of the objective space is displayed in Figures 7, 8, 9, and 10. Again, these univariate samplings consider 10 consecutive simulations to display mean and standard deviation. For P, a, and i the constellation size is fixed, thus only considering the object detection objective function. When varying N, the lifecycle cost increases in the same manner shown in Figure 3. Daily unique detections are also provided in terms of percentage of the current SOC and are shown within 3 sigma.

With changing semi-major axis, it can be seen that higher altitudes are more favorable in general. RSOs in lower altitude orbits decay more quickly, meaning that much of the persistent population of RSOs are at higher LEO altitudes. Higher altitude orbits are closer to these more densely packed regions, making detection more attainable. Another potential explantion to the increased performance of larger semi-major axis is the reduction in the line of sight detection constraint given the pole pointing CONOPS. Higher altitude orbits will have a clearer view of the dense pole regions for longer periods of time, leading to increased number of detections.

When changing inclination a clear optimum can be seen at 60 degrees. Knowing that the poles represent the areas of largest spacial density of objects, one might expect higher inclination orbits to be favored. However, given the pole

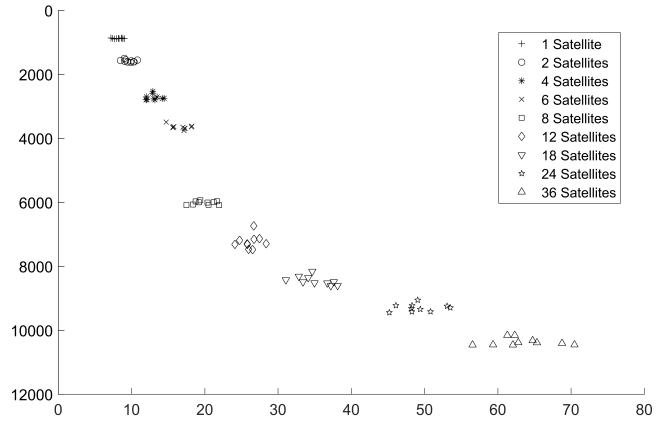

Figure 6. Pareto frontier of multiple objectives with aggregate cumulative density function

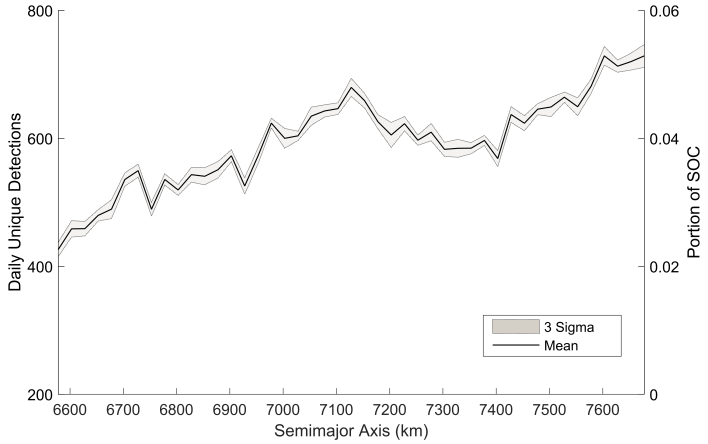

Figure 7. Detections of a Single Satellite at 70° Inclination

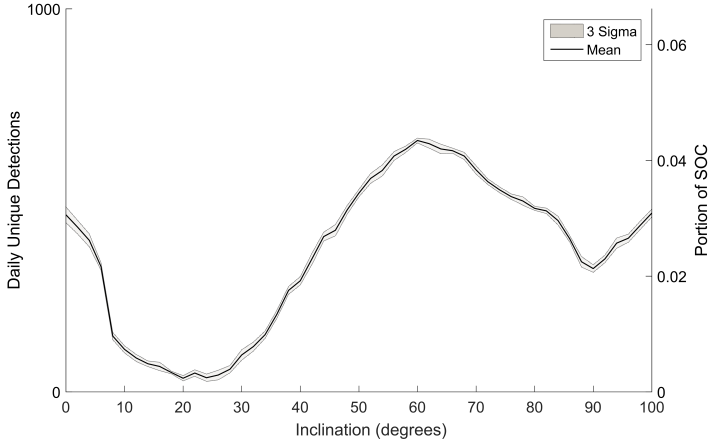

Figure 8. Detections of a Single Satellite at 500 km Orbital Altitude

pointing CONOPS, these higher inclination orbits experience higher relative velocity and angular rates with respect to RSOs, making detections more difficult. This can clearly be seen by the local minima at 90 degrees. In addition to the 60 degree maxima, it is interesting to note the local maxima at the equatorial plane. Knowing that the CONOPS used here points towards GEO when the pole pointing target is out of view, these increased detections are presumably GEO RSOs.

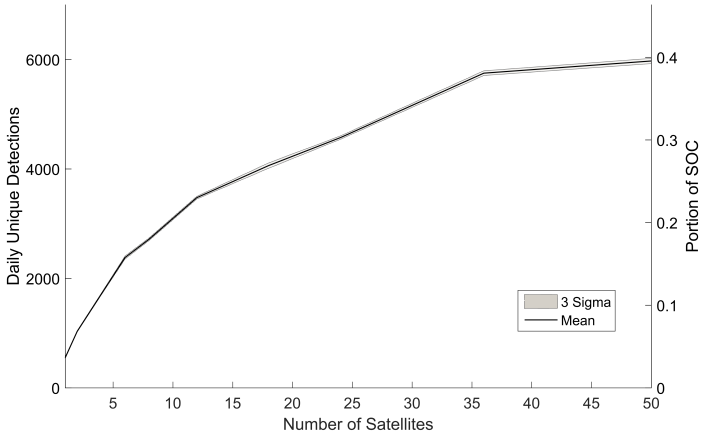

Figure 9. Detections of a Single Plane Constellation at 500 km Orbital Altitude and 70° Inclination

Within a single plane, the number of satellites is directly related to the quantity of detections, as should be expected. This configuration could be achieved by a large cluster launch on a single launch vehicle. Though the number of objects detected increases with constellation size, there are diminishing returns. It should be expected that with very large constellations, the number of unique observations would approach an asymptote, as is suggested by the final data point at 50 satellites. Because of this performance, the maximum 36 satellite constellation size considered in the optimization algorithm seems acceptable.

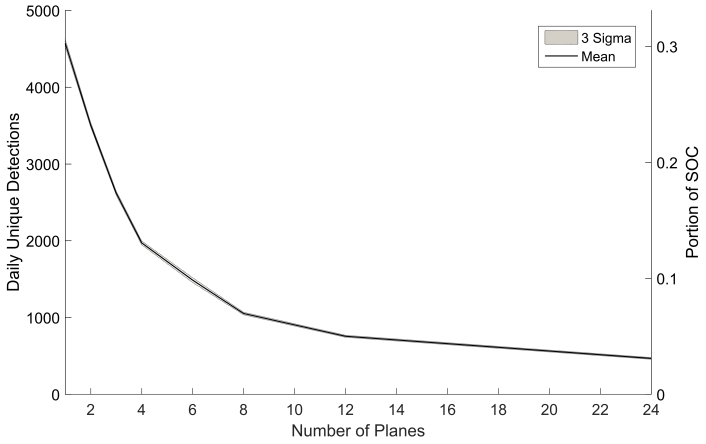

Figure 10. Detections of a 24 Satellite Constellation at 500 km Orbital Altitude and 70° Inclination

Finally, the configuration of a fixed constellation size can be analyzed by a univariate search across multiple orbital planes. While keeping N constant, increasing P decreases S proportionally. With a constellation of 24 satellites at 500 km and 70°, a constellation in a single plane is significantly favored over multi-plane constellations. This behavior is the direct result of the pole pointing CONOPS. Since this region is the most densely populated, an equally

phased train of satellites will be able to more consistently monitor this region at a given phase angle with little overlap. Though the arguments of periapsis in multi-plane Walker delta constellations are similarly phased, the the additional planes experience poor solar phase angles thus reducing their performance.

Note that for all design points a large percentage of the current SOC is observed every day. The previously operational Space Fence consistently monitored 40% of the SOC on a daily basis [39]. The constellations considered here are capable of detecting roughly 10% to 30% of the SOC in a given day at a price point of $10M to $100M. Though the there should be significant systemic uncertainty with relation to modeling the cost of CubeSat missions, the cost order of magnitude is attractive.

B. Discussion of Results

This optimization exercise yields some interesting results that are worth analyzing for the sake of future mission planners. In addition to the plots, the final design configurations of the 90 optimization algorithms are provided in Appendix B. These design points can be used to as a starting point for mission designers. In order to apply some of the results presented here, a discussion of two additional mission objectives are discussed here.

First, a mission planner must understand the impact of cost and performance efficiency along the Pareto frontier of varying constellation sizes. Smaller constellations are less expensive, but larger constellations are more efficient in terms of lifecycle cost per observation. If daily unique detections remain constant through time, a year long campaign could provide relative performance parameters of $25.6/daily unique detection for a single satellite constellation and as low as $16.75/daily unique detection for 36 satellites. These cost efficiency numbers could be further reduced by extending the lifecycle of the mission; however, it should be expected that CubeSat missions will have a shorter lifespan that traditional SSA missions. Depending on the financial objectives of mission planners, either of these designs may be preferable. A smaller constellation could be a low cost supplement to larger SSA efforts, whereas a larger constellation could present an opportunity for an efficient and repeatable SSA campaign. Stated again, the mean single satellite constellation will detect 5.8% of the current SOC per day for a lifecycle cost of $8.2 million, and the mean 36 satellite constellation will detect 68.6% of the SOC per day for $63.8 million.

In this optimization effort, the primary performance method considered is the daily unique detections with the ultimate objective for broad detection. Some mission planners may seek to favor accuracy or frequency of detection over unique detections. To further understand these dynamics, one of the optimal constellation configurations point at the ”knee” of the Pareto frontier is considered. This constellation consists of 8 satellites in 2 orbital planes at 929 km and 68.7 degrees. Of the 15,106 RSOs simulated, this constellation achieved 4,311 unique detections over 24 hours. For these detected objects, Figure 11 shows the number of repeat detections. During this period, the constellation detected each object an average of 2.5 times and as high as 38 times for certain objects. For close monitoring of specific objects, these repeat detections could be further improved.

Though many SSA efforts seek to detect as many objects as possible, some mission planners may wish to specifically focus on particular regions. Figure 11 also categorizes the orbital locations of these detected objects based on the classification shown in Appendix A. Not surprisingly, LEO spacecraft in polar orbits are most frequently detected given the CONOPS employed here. However, this mission plan could be altered for the sake of monitoring specific regions more closely.

Though the specific objectives of mission planners may vary, this paper illustrates the potential for CubeSat SSA constellations. Even though dis-aggregated constellations present certain operational and organizational challenges as compared to flagship missions, the low cost nature of CubeSat systems present an attractive mission design that could be used as a meaningful supplement to flagship efforts.

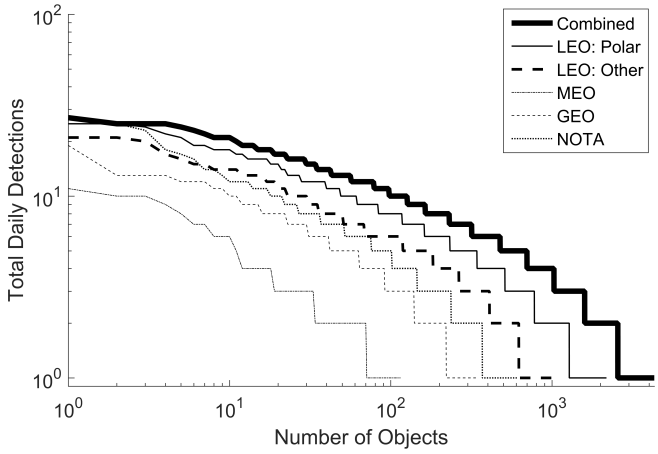

Figure 11. Repeat Detections of a 8 Satellite Constellation at 979 km Orbital Altitude and 68.7° Inclination

IV. Conclusion

This paper begins with a formal definition of the geometrically detectable volume for a space-based observer. By augmenting this volume to include the capabilities of a given electro-optical sensor (EOS) a true detectable volume of state space is defined using the concept of probability of detection. Mission design is formulated as an idealized optimization problem with the objective of maximizing the fractional coverage of space object distributions. Describing mission design as an optimization problem then enables the formal definition of the basic concept of operations for a general space-based, disaggregated space situational awareness (SSA) mission. Additionally, this approach incorporates the optimization of the spacecraft design parameters which is demonstrated through the design and sizing of a CubeSat EOS payload. This optimization problem is generally computationally intractable due to the high dimensionality and the number of design parameters. By constraining the concept of operations and the spacecraft optical parameters, the optimization problem is reduced to a computationally tractable optimization problem. A CubeSat constellation cost model is developed to evaluate the cost of a given architecture. Using both detection performance and lifecycle cost in a multi-objective optimization problem, a Pareto frontier of constellation design tradeoffs is developed. The results of this optimization effort are further discussed in there potential application to future SSA missions. The analysis considered here suggests that a CubeSat SSA constellation can be a cost effective alternative and meaningful supplement to large scale missions.

V. Supporting Material

The continued and effective use of Earth orbit for all purposes, including commercial and governmental, requires a low Earth orbit (LEO) environment that can be accurately characterized. The growth of space debris over recent years has made such characterization difficult. Fragmentations of rocket bodies, active satellites, and defunct satellites, among other things, have created huge numbers of resident space objects (RSOs) that are very difficult to track [1].

The majority of data on RSOs comes from the US Department of Defense Joint Space Operations Center (JSpOC). This data is gathered through the Space Surveillance Network (SSN) that JSpOC tasks with the observation and tracking of RSOs. The SSN consists of a network of approximately 30 ground- and space-based sensors that detect and track objects in Earth orbit [2]. Data from the SSN for all non-classified objects is then made publicly available in the form of two line elements (TLEs) via Space-track.org. There are currently in excess of 21,000 LEO objects with diameters above 10 cm [3] in the JSpOC space object catalog (SOC). The TLEs for approximately 15,106 of these objects are publicly available[b]. The largest contributions to the SSN are ground-based systems that use either electro-optical sensors (EOS) or radar [4]. For radar based systems, which are by far the largest contributors to the SSN, Rayleigh scattering makes debris smaller than 10 cm in diameter very difficult to reliably track [5]. As such, the number of objects in LEO below 10 cm is presently only estimated. Current estimates place the number of objects larger than 1 cm at approximately 700,000 and the number of objects larger than 1 mm at approximately 200 million [6]. A quick analysis of JSpOC numbers on functional vs. nonfunctional Earth satellites reveals that only around 7% of RSOs are operational assets; in essence, 93% of the objects in orbit about Earth serve to do nothing other than limit and endanger on-orbit assets [7].

The situation continues to worsen at a concerning rate. Events such as the 2007 Anti-Satellite (ASAT) test on the defunct Fengyun-3 weather satellite [8] and the 2009 collision between the defunct Cosmos-2251 and the operational Iridium-33 [9] have both significantly worsened the problem. These two events alone doubled the number of space objects larger than 1 cm, producing over 250,000 new fragments [10]. Continuing ASAT tests [11] will only continue to worsen the situation. Orbital debris larger than 10 cm in diameter can cause catastrophic failure in most space missions, and debris in the 1 to 10 cm regime can easily disable or damage core mission functionality [12]. Damage from debris in the 1 to 10 cm regime has posed a catastrophic risk to the Space Shuttle on multiple occasions [13, 14]. It has been established that should a critical density of orbital debris be reached, cascading collisions of debris could have the potential to create a debris belt in Earth orbit. [15]. Such a debris belt would have terrible consequences to the feasibility of future space missions. In order to understand actions that should be taken to properly address the likelihood of this eventuality, the situation must be assessed before it becomes untenable.

[b] via www.space-track.org; accessed 3/30/2015

There is currently action being taken via many different avenues. Space situational awareness (SSA), the characterization of the space domain, has been listed as a priority for research and technology advancement at many levels of the United States government. The Presidential Space Policy under the administration of U.S. President Barack Obama calls for increased knowledge of the space environment [16]. The Presidential Space Policy has informed the policy of the Joint Chiefs of Staff in Joint Publication 3-14, which recognizes increased SSA as one of the most important areas for increased research and new technology in the coming decade [17, 18]. As a result, the recent FY2016 US Defense Budget Request includes increases in funding to the Space Based Space Surveillance (SBSS) mission and the JSpOC Mission System (JMS) [19]. Recognizing the issue on a global scale, the United Nations Committee on the Peaceful Uses of Outer Space also promotes international cooperation on SSA as it is an issue that affects all space-faring nations [20].

Given the worsening problem in LEO and the clear need for increased SSA, especially regarding objects with diameters from 1 to 10 cm, it is evident that much work remains regarding RSO detection. Due to their recent proliferation, opportunities exist in the application of small satellite design paradigms to RSO detection.

Debris detection was first performed with ground-based radars, and radar systems continue to be used for this purpose. Ground-based approaches can be divided between optical imaging and radar imaging. Typically, optical imaging performs much better for objects in geosynchronous Earth orbit (GEO) while radar is better for the observation of objects in LEO [21]. The earliest attempt at RSO detection was the radar detection of Sputnik with the Millstone radar at MIT Lincoln Laboratory's Millstone Hill observatory [22]. Very accurate radar observations of small diameter RSOs are still made at this site with the MIT Lincoln Laboratory Haystack radar [23], one of the first dedicated contributors to the SSN. One of the most recent ground-based radar contributors to the SSN is the Space-Fence radar array, which is designed to make approximately 1,500,000 observations of LEO objects each day [4]. Detections of debris smaller than 10 cm have been made with ground-based radar [24, 25], but such observations cannot be made accurately and consistently enough to contribute to the JSpOC SOC. Deep space radar observatories on the Kwajalein atoll have also been successful in the accurate tracking of GEO objects [22].

Ground-based optical approaches for debris detection have been increasingly employed. The most notable of these approaches have been the Optical Ground Station (OGS) [26] and, more recently, the Space Surveillance Telescope (SST) [27]. Both observatories have made substantial contributions to the characterization of the GEO debris environment. Other ground-based optical approaches have involved the repurposing of astronomical telescopes for the observation of LEO debris. Notable examples of this can be found in [28, 29, 30, 31] as summarized by Shell in [32]. However, given that ground-based optical observatories are most effectively applied to GEO observations, their limitation lies in the fact that they are only able to characterize a small portion

of the GEO debris belt that is visible from their fixed location. While their observations can be extrapolated to estimate numbers of GEO debris, they cannot be used to actively catalog it.

Space-based systems offer different design paradigms than ground-based systems because of their relative proximity to RSOs. One such advantage is the ability to physically detect the impact of extremely small debris and thus measure its presence. The first approaches in this manner include the Long Duration Exposure Facility [33], the Particle Impact Experiment on MIR [34] and evidence of debris impact on the space shuttle [14]. An exhaustive review of impact-related in-situ detection is presented by Bauer et al. in [6]. By nature, such experiments are unable to catalog debris above certain size limits and debris that is still in orbit and therefore can contribute only to statistical models of the debris environment rather than track orbits of individual objects for the SOC.

Space-based radar has not traditionally been applied due to the fact that the use of radar detection requires large structures and high power, both of which make its application exceedingly difficult in a space environment. No missions have successfully carried out the space-based radar detection of orbital debris. The only plans to do so are theoretical [35].

The application of space-based optical imaging systems to on-orbit debris detection has been very successful. The earliest such mission, the Midcourse Space Experiment (MSX) Space Based Visible (SBV) detector [36] demonstrated effective maturation of the technology necessary for such a mission, and serves as a design standard for space based optical detection mission architectures. The Sapphire mission [37], Space-based Telescopes for Actionable Refinement of Ephemeris (STARE) mission [38] and SBSS mission [39] not only use optical sensors to make on-orbit detections of space debris, but also do so with a similar concept of operations (CONOPS) as the MSX/SBV mission. The MSX/SBV mission proved the design paradigm of placing a sensor in LEO and alternating the data collection of LEO and GEO objects with the data processing of the same objects for downlink to the ground [40]. The Sapphire, STARE, and SBSS missions all do the same. The MSX/SBV, Sapphire, and SBSS missions are also all capable of both tasked and passive observation of RSOs. However, all three of these missions are much larger than the STARE mission. The STARE mission, a 3U CubeSat, is the first and only current application of the CubeSat form factor to RSO detection. However, even though it is much smaller than similar missions, a review of its optical payload [41] and CONOPS [42] reveals few differences in effectiveness or application.

In fact, CubeSats offer much more potential than other mission architectures for the detection of RSOs as their low cost and ease of scalability allows them to be added to a constellation more easily and to adapt to changes in technology more quickly [43]. A constellation is also much more resistant to faults as it is fractionated and disaggregated; a failure of one unit does not result in the failure of the entire system. Planet Labs has recently begun the deployment of a ground-observing CubeSat constellation in LEO [44]. Similar constellation architectures could be adapted for SSA.

A disaggregated system offers many benefits for system redundancy and efficacy [45], but a disaggregated design paradigm has only recently begun to be employed. The SBSS mission is planned to scale to a constellation of satellites, but has yet to be fully deployed. Likewise, Space Fence, one of the most recent approaches to ground-based radar detection, consists of two ground-based radar arrays, but is not planned to scale any further [4]. In short, while many mission architectures do exist to characterize the current situation of debris in Earth orbit, few mission architectures effectively do so in a disaggregated and easily scalable manner.

A constellation may be optimized for debris detection. Genetic algorithms are well-suited to this problem because of their ability to fully explore an entire design space. Many constellation optimization problems have been addressed using genetic algorithms [46, 47, 48, 49]. As such, the use of such applicable methodology for optimizing a system of debris observing satellites is well established. Additionally, the use of a constellation allows for the standardization of data processing and can streamline the contributions of a system to the SSN [50].

This paper introduces an abstraction of the constellation design problem for a space-based optical debris observation system. The formulation presented has the inherent value of being written in provably true logical statements rather than being based on a designer's intuition. These provably true statements relate all parameters of a system to mission performance and thus allow for the optimization of mission performance based on parameters of the system. Geometric line of sight, object illumination, and field of view detection constraints are all taken into account and related to mission success criteria. This paper serves as a guide for this design problem.

The performance of such a system cannot be computationally analyzed if every design parameter is allowed to vary simultaneously, as the problem would simply be too large. Therefore, this paper applies a series of assumptions based on physical and technological constraints to this design problem, allowing for an approximate analysis and optimization of the entire constellation to be carried out. To be able to simulate the performance offered by a given constellation, assumptions can be made regarding many parameters so that they are constrained to the realm of possibility. Given a CubeSat form factor, the size of detection sensors can be constrained and performance capabilities can be determined. After the performance of an individual satellite is analyzed, a multi-objective optimization algorithm (MOO) is applied to parametrically optimize a constellation of these satellites with respect to mission performance and lifecycle cost. The objective function corresponding to mission performance is the fractional coverage of the orbital debris that is currently available in the JSpOC SOC, and the objective function for lifecycle cost is defined using traditional cost estimating principles. The epsilon constraint method is used to formulate the MOO problems a series of single objective optimizations. These optimization methods are used to develop the Pareto frontier of constellation designs.

In short, the contributions of this effort are the formal definition of a constellation and CONOPS design for disaggregated space-based SSA, a discussion of the application of SSA sensor sizing

and data processing, and a MOO problem for constellation design.

VI. The Constellation and Concept of Operations Design Problem

A CubeSat SSA constellation and CONOPS design is fundamentally focused on detecting, tracking, and characterizing as many space objects as possible. This is inherently a multi-objective problem; in many cases tracking and characterization efforts directly oppose new object detection efforts. For example, detecting new objects necessarily reduces resources available for tracking existing objects.

Constellation design is a challenging high-dimensional multi-objective optimization problem that has motivated the formulation of a number of specific constellation types, including Walker [51], Beste [52], Ballard [53], Molniya [54], Draim [55, 56], and Flower [57, 58] constellations. Selected design considerations include geographic coverage, redundancy of coverage, coverage quality, ground station connectivity, communication satellite connectivity, orbit insertion methods, orbit error tolerance, orbit perturbation tolerance, and constellation survivability [59]. Parameterization of these constellation types helps attenuate the staggering difficulty of designing and assessing the performance of a constellation with N individual satellites. In practice for computational tractability, most constellations reduce the design problem down to only a few decision variables (e.g., altitude, inclination, phasing) [59].

This section intends to develop a simplified version of the space-based SSA constellation, CONOPS, and CubeSat design problem to enable future rigorous studies in this area and to place the remainder of this paper in perspective. Similar to the parameterization of constellations, the combined SSA CONOPS / CubeSat constellation design problem is, by assumption, reduced to a numerically tractable set of decision variables. Emphatically, the full design problem proves computationally intractable and is not solved in its general form in this paper.

Constellation design is often a combination of nonlinear continuous and mixed integer optimization problems. Solution to constellation design problems often takes years and hundreds or thousands of design iterations [59]. In the interest of tractability, this paper considers the CONOPS design to be answered by a combination of inertial state and attitude profiles for nominal mission operational status over some finite period of time. Said differently, here the CONOPS is limited to the location and pointing of the spacecraft and sensors over a finite period of time.

The sensor types considered in this analysis are passive electro-optical sensors (EOS) that measure phenomenologies related to the presence or absence of space objects on orbit. In particular, an EOS is defined here as any electronic device that generates discrete-event signals triggered by photon events. As a group, EOS sensors include Charge-Coupled Devices (CCDs), Complementary Metal Oxide Semiconductor (CMOS) sensors, and photon counting devices. This section first briefly describes geometric constraints, and introduces the approximate statistics behind the detection of space objects. Next, a single performance objective function - the number of unique space

object detections in a given finite time period - is derived and the resulting problem discussed. Finally, solution challenges are identified and an overarching solution strategy for design of a SSA Constellation of CubeSats is articulated.

A. Problem Geometry and Visualization

The overall space object detection geometry is illustrated in Figure 12a. The line-of-sight vector

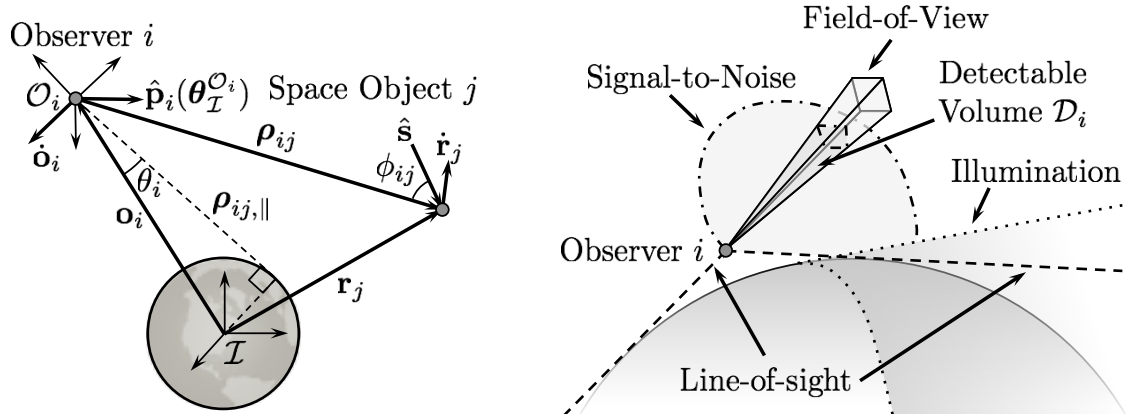

a) Observer i and space object j geometry. **b) Visualization of detectable volume $\mathcal{D}_i$**

Figure 12. Problem Geometry and Constraint Visualization

$\boldsymbol{\rho}_{ij} = \mathbf{r}_j - \mathbf{o}_i$, where $\mathbf{r}_j$ is the j^{th} RSO inertial location and $\mathbf{o}_i$ is the i^{th} observer (sensor platform) location. Additionally, $\hat{\mathbf{s}}$ is defined as the sun-vector (pointing away from the sun) and ϕ_{ij} is defined as the solar phase angle of the j^{th} RSO as seen by observer i. The i^{th} observer's EOS has a defined boresight $\hat{\mathbf{p}}_i(\boldsymbol{\theta}_{\mathcal{N}}^{\mathcal{O}_i})$, where $\boldsymbol{\theta}_{\mathcal{N}}^{\mathcal{O}_i}$ defines a rotation in the rotation group SO(3) from the inertial frame $\mathcal{N}$ to the i^{th} EOS boresight frame $\mathcal{O}_i$.

The j^{th} RSO position $\mathbf{r}_j$ and velocity $\dot{\mathbf{r}}_j$ are collectively referred to as the state $\mathbf{x}_j^T = \left[\mathbf{r}_j^T,\ \dot{\mathbf{r}}_j^T\right]$. Similarly, the observing platform state is written as $\mathbf{x}_{o,i}^T = \left[\mathbf{o}_i^T,\ \dot{\mathbf{o}}_i^T\right]$. The states $\mathbf{x}_j$ and $\mathbf{x}_{o,i}$ are restricted over a domain $\mathcal{X}$ such that $\mathbf{x}_j, \mathbf{x}_{o,i} \in \mathcal{X} \subseteq \mathbb{R}^6$. Intuitively, not all possible states $\mathbf{x}_j$, $\mathbf{x}_{o,i}$ in $\mathcal{X}$ lead to a detection by an an EOS on observer i at every instant t, reducing the set of states that may be detected to $\mathcal{D}_i \subseteq \mathcal{X} \subseteq \mathcal{R}^6$. A notional visualization of selected constraints is given in Figure 12b. Several such constraints are formally introduced in the following subsections. While these constraints are not novel and represent a combination of common sense and recent work [60], their inclusion here is necessary for notational purposes and to support a formal articulation of the objective function and optimization problem in §VI. G. In the interest of brevity variables that are not considered optimization decision variables are omitted from formal functional definitions.

B. Line-of-Sight

The observer must have Line of Sight (LoS) to a space object for a detection to occur. The region of space in which the observer does not have LoS is a cone extending from the observer encompassing

Earth's surface. Using the notations shown in Figure 12a, for the i^{th} observer the angle θ_i between the tangent vector $\boldsymbol{\rho}_{ij,\|}$ and $\mathbf{o}_i$ defines the half-angle of this exclusion cone. The Earth radius vector is written as $\mathbf{R}_e$ and the vector $\boldsymbol{\rho}_{ij,\|}$ and $\mathbf{o}_i$ completes the vector triangle with $\mathbf{o}_i$. Noting the geometry shown in Figure 12a and that $\|\mathbf{R}_e\|^2 + \|\boldsymbol{\rho}_{ij,\|}\|^2 = \|\mathbf{o}_i\|^2$, the equation describing the line of sight constraint for space object j is written after some manipulation as

$$\kappa_{i,\mathcal{L}_i}(\mathbf{o}_i, \mathbf{r}_j) = -\mathbf{o}_i \cdot \hat{\boldsymbol{\rho}}_{ij} - \sqrt{\|\mathbf{o}_i\|^2 - \|\mathbf{R}_e\|^2} \leq 0 \tag{19}$$

where $\kappa_{i,\mathcal{L}} : \mathbb{R}^3 \times \mathbb{R}^3 \to \mathbb{R}$. Thus, if Eqn. (19) is true then the observer i has LoS with object j and the following comprises the subset of $\mathcal{X}$ that has LoS with the observer i^{th}.

$$\mathcal{L}_i := \{\mathbf{r}_j \in \mathbb{R}^3 \mid \kappa_{i,\mathcal{L}}(\mathbf{o}_i, \mathbf{r}_j) \leq 0\} \tag{20}$$

The LoS constraint operates on the position subspace and may be expressed as $\mathbf{r}_j \in \mathcal{L}_i(\mathbf{o}_i) \subseteq \mathbb{R}^3$. Because RSO velocity is irrelevant for this constraint, the state space constraint may be formally expressed as $\mathbf{x}_j \in \mathcal{L}_i \times \mathbb{R}^3 \subseteq \mathbb{R}^6$.

C. Field-of-View

The Field-of-View (FOV) constraint ensures the space object is in the FOV of the sensor. In general, an EOS has a rectangular field of view. Thus FOV_h and FOV_v are defined as the horizontal and vertical field of view angles (full angle, not half-angle) of the observer, respectively. The i^{th} observer sensor boresight in the inertial frame is written as $\hat{\mathbf{p}}_i(\boldsymbol{\theta}_{\mathcal{N}}^{\mathcal{O}_i})$. The geometric constraints expressed in the local boresight frame $\mathcal{O}_i$ of the i^{th} observer may be written as a combination of separating hyperplane constraints outlining the EOS FOV. Individually, such a hyperplane implicitly defined by a normal vector $\hat{\mathbf{a}}_{i,l}$ may be expressed as

$$\hat{\mathbf{a}}_{i,l}^T \boldsymbol{\rho}_{ij} \geq 0 \tag{21}$$

$$\hat{\mathbf{a}}_{i,l}^T (\mathbf{o}_i - \mathbf{r}_j) \leq 0 \tag{22}$$

where there are a total of f constraints forming the FOV. Because ${}^{\mathcal{O}_i}\hat{\mathbf{a}}_{i,l} = \mathbf{R}(\boldsymbol{\theta}_{\mathcal{N}}^{\mathcal{O}_i})\hat{\mathbf{a}}_{i,l}$, with $\mathbf{R}(\boldsymbol{\theta}_{\mathcal{N}}^{\mathcal{O}_i})$ being a right-handed rotation matrix from the inertial frame $\mathcal{N}$ to the sensor frame $\mathcal{O}_i$, (22) may be re-written as

$${}^{\mathcal{O}_i}\hat{\mathbf{a}}_{i,l}^T \mathbf{R}(\boldsymbol{\theta}_{\mathcal{N}}^{\mathcal{O}_i}) (\mathbf{o}_i - \mathbf{r}_j) \leq 0 \tag{23}$$

Since there are f such constraints ($l = 1, \ldots, f$), the field of view constraint is written as

$$\begin{bmatrix} {}^{\mathcal{O}_i}\hat{\mathbf{a}}_{i,1}^T \\ \vdots \\ {}^{\mathcal{O}_i}\hat{\mathbf{a}}_{i,f}^T \end{bmatrix} \mathbf{R}(\boldsymbol{\theta}_{\mathcal{N}}^{\mathcal{O}_i}) \left(\mathbf{o}_i - \mathbf{r}_j\right) \leq \mathbf{0} \tag{24}$$

or, equivalently,

$$\boldsymbol{\kappa}_{i,\mathcal{F}}(\mathbf{o}_i, \mathbf{r}_j, \boldsymbol{\theta}_{\mathcal{N}}^{\mathcal{O}_i}) = \mathbf{A}_i(\boldsymbol{\theta}_{\mathcal{N}}^{\mathcal{O}_i})\mathbf{o}_i - \mathbf{A}(\boldsymbol{\theta}_{\mathcal{N}}^{\mathcal{O}_i})\mathbf{r}_j \leq \mathbf{0} \tag{25}$$

with $\boldsymbol{\kappa}_{i,\mathcal{F}} : \mathbb{R}^3 \times \mathbb{R}^3 \times \mathrm{SO}(3) \to \mathbb{R}^f$. Using this formulation, a number of separating hyperplanes result in an inequality constraint that is nonlinear in the observer attitude coordinate $\boldsymbol{\theta}_{\mathcal{N}}^{\mathcal{O}_i}$, but linear in both $\mathbf{o}_i$ and $\mathbf{r}_j$. The set of $\mathbf{r}_j$ that satisfy this constraint given $\mathbf{o}_i$ and $\boldsymbol{\theta}_{\mathcal{N}}^{\mathcal{O}_i}$ is formally defined as

$$\mathcal{F}_i := \left\{\mathbf{r}_j | \boldsymbol{\kappa}_{i,\mathcal{F}}(\mathbf{o}_i, \mathbf{r}_j, \boldsymbol{\theta}_{\mathcal{N}}^{\mathcal{O}_i}) \leq \mathbf{0}\right\} \tag{26}$$

Since this constraint depends only on position, the full RSO state $\mathbf{x}_j \in \mathcal{F}_i \times \mathbb{R}^3$.

D. Illumination

To be detected by a passive EOS, the RSO in question must be illuminated by an external source (typically the sun). Given the sun vector $\hat{\mathbf{s}}$, an object j that is not eclipsed by the Earth must satisfy the two approximate conditions shown in Equations (27) and (28), where again R_e is the radius of the Earth.

$$\mathbf{r}_j \cdot \hat{\mathbf{s}} \leq 0 \tag{27}$$

$$\|\hat{\mathbf{s}} \times \mathbf{r}_j \| \ \geq R_e \tag{28}$$

Eqns. (27) and (28) may be written in constraint form as

$$\kappa_{\mathcal{I},1}(\mathbf{r}_j) = \mathbf{r}_j \cdot \hat{\mathbf{s}} \tag{29}$$

$$\kappa_{\mathcal{I},2}(\mathbf{r}_j) = R_e - \|\hat{\mathbf{s}} \times \mathbf{r}_j\| \tag{30}$$

Where the constraint functions $\kappa_{\mathcal{N},\cdot} : \mathbb{R}^3 \times \mathbb{R}^3 \to \mathbb{R}$ must both be simultaneously satisfied for RSO j to be illuminated. Thus the subset of $\mathcal{X}$ containing objects illuminated by the Sun is given by

$$\mathcal{I} := \{\mathbf{r}_j \in \mathbb{R}^3 \mid \ (\kappa_{\mathcal{I},1}(\mathbf{r}_j) \leq 0) \cup (\kappa_{\mathcal{I},2}(\mathbf{r}_j) \leq 0)\} \tag{31}$$

Again, this is a position constraint, and the subspace of positions that are illuminated may be written as $\mathbf{r}_i \in \mathcal{I} \subseteq \mathbb{R}^3$. Because velocity does not affect illumination, the full state space constraint becomes $\mathbf{x}_j \in \mathcal{I} \times \mathbb{R}^3$. As a note, Earthshine or Lunar albedo may be considered using similar

formulations. Further, the illumination constraint depends in no way on the observer location $\mathbf{o}_i$.

E. Geometric Detectability

For an EOS i to be geometrically capable of detecting RSO j, the LoS, FOV, and illumination constraints must all be satisfied. This is represented notationally by requiring that $\mathbf{r}_j \in \mathcal{D}_i(\mathbf{x}_{o,i}, \boldsymbol{\theta}_{\mathcal{N}}^{\mathcal{O}_i})$, where $\mathcal{D}_i(\mathbf{x}_{o,i}, \boldsymbol{\theta}_{\mathcal{N}}^{\mathcal{O}_i}) \equiv \mathcal{L}_i \cap \mathcal{F}_i \cap \mathcal{I}$. The full state-space constraint for the j^{th} RSO is $\mathbf{x}_j \in \mathcal{D}_i(\mathbf{x}_{o,i}, \boldsymbol{\theta}_{\mathcal{N}}^{\mathcal{O}_i}) \times \mathbb{R}^3 \subset \mathcal{X}$. However, even if a RSO j is geometrically detectable by EOS i (i.e., $\mathbf{x}_j \in \mathcal{D}_i(\mathbf{x}_{o,i}, \boldsymbol{\theta}_{\mathcal{N}}^{\mathcal{O}_i}) \times \mathbb{R}^3$), the RSO, EOS, and scenario characteristics must still be accounted for when computing the probability that a detection occurs. This is discussed in the following subsection.

F. Space Object Detection Probability

As demonstrated by Coder & Holzinger [61], the probability of detection for the j^{th} space object moving relative to the i^{th} sensor frame is

$$p_{ij,d}(t_I;\cdot) \approx \frac{1}{2}\left[1 - \text{erf}\left(\frac{\text{SNR}_{i,\text{alg}}\sqrt{q_{j,\text{RSO}}t_I + m_{ij}\left(1+\frac{1}{z_{ij}}\right)\left[(q_{i,\text{p,bkg}} + q_{i,\text{p,dark}}) + \frac{\sigma_{i,r}^2}{n_i^2}\right]} - q_{j,\text{RSO}}t_I}{\sqrt{2q_{i,\text{RSO}}t_I}}\right)\right] \tag{32}$$

where $\text{SNR}_{i,\text{alg}}$ is the signal-to-noise ratio required by the detection algorithm, $q_{j,\text{RSO}}$ is the EOS count rate generated by the j^{th} space object, $t_{I,i}$ is the i^{th} EOS integration period, m_{ij} is the number of pixels the space object streak covers, z_{ij} is the number of pixels over which the background noise is determined, $q_{\text{i,p,bkg}}$ is the per-pixel EOS count rate due to background sources, $q_{\text{i,p,dark}}$ is the per-pixel count rate due to dark current, $\sigma_{i,r}$ is the EOS read noise, and n_i is the number of image frames per integration period t_I. The EOS count rate $q_{j,\text{RSO}}$ is a function of the RSO shape, surface materials, inertial location $\mathbf{r}_j$, and attitude. A full discussion is given by Holzinger, et al. [62]. The number of pixels m_{ij} over which the space object signature is spread may be approximated over short time periods as

$$m_{ij} = m_{ij,0} + \sqrt{m_{ij,0}}\left(\frac{\dot{\eta}_{ij}t_I}{\text{IFOV}_i}\right) \tag{33}$$

where $m_{ij,0}$ is the spot size of the space object (including diffraction, jitter, and other sources), $\dot{\eta}_{ij}$ is the apparent angular rate, and IFOV_i is the instantaneous pixel field of view. The instantaneous apparent angular rate as seen by a frame $\mathcal{O}_i$ fixed to the i^{th} EOS boresight rotating with angular

velocity $\boldsymbol{\omega}_{\mathcal{N}}^{\mathcal{O}_i}$ with respect to the inertial frame $\mathcal{N}$ is given by

$$
\begin{aligned}
{}^{\mathcal{O}_i}\frac{\mathrm{d}\hat{\boldsymbol{\rho}}_{ij}}{\mathrm{d}t} &= {}^{\mathcal{N}}\frac{\mathrm{d}\hat{\boldsymbol{\rho}}_{ij}}{\mathrm{d}t} + \boldsymbol{\omega}_{\mathcal{N}}^{\mathcal{O}_i} \times \hat{\boldsymbol{\rho}}_{ij} && (34)\\
{}^{\mathcal{O}_i}\frac{\mathrm{d}\hat{\boldsymbol{\rho}}_{ij}}{\mathrm{d}t} &= \frac{1}{\|\boldsymbol{\rho}_{ij}\|}\left[\mathbb{I} - \frac{\boldsymbol{\rho}_{ij}\boldsymbol{\rho}_{ij}^T}{\boldsymbol{\rho}_{ij}^T\boldsymbol{\rho}_{ij}}\right]{}^{\mathcal{N}}\frac{\mathrm{d}\boldsymbol{\rho}_{ij}}{\mathrm{d}t} + \boldsymbol{\omega}_{\mathcal{N}}^{\mathcal{O}_i} \times \left[\frac{\mathbf{r}_j - \mathbf{o}_i}{\|\mathbf{r}_j - \mathbf{o}_i\|}\right] && (35)\\
{}^{\mathcal{O}_i}\frac{\mathrm{d}\hat{\boldsymbol{\rho}}_{ij}}{\mathrm{d}t} &= \frac{1}{\|\boldsymbol{\rho}_{ij}\|}\left[\mathbb{I} - \frac{\boldsymbol{\rho}_{ij}\boldsymbol{\rho}_{ij}^T}{\boldsymbol{\rho}_{ij}^T\boldsymbol{\rho}_{ij}}\right](\dot{\mathbf{r}}_j - \dot{\mathbf{o}}_i) + \boldsymbol{\omega}_{\mathcal{N}}^{\mathcal{O}_i} \times \left[\frac{\mathbf{r}_j - \mathbf{o}_i}{\|\mathbf{r}_j - \mathbf{o}_i\|}\right] && (36)\\
\rightarrow \left\|{}^{\mathcal{O}_i}\frac{\mathrm{d}\hat{\boldsymbol{\rho}}_{ij}}{\mathrm{d}t}\right\| \equiv \dot{\eta}_{ij} &= \left\|\frac{1}{\|\boldsymbol{\rho}_{ij}\|}\left[\mathbb{I} - \frac{\boldsymbol{\rho}_{ij}\boldsymbol{\rho}_{ij}^T}{\boldsymbol{\rho}_{ij}^T\boldsymbol{\rho}_{ij}}\right](\dot{\mathbf{r}}_j - \dot{\mathbf{o}}_i) + \boldsymbol{\omega}_{\mathcal{N}}^{\mathcal{O}_i} \times \left[\frac{\mathbf{r}_j - \mathbf{o}_i}{\|\mathbf{r}_j - \mathbf{o}_i\|}\right]\right\| && (37)
\end{aligned}
$$

Thus, the probability $p_{ij,d}$ of EOS i detecting RSO j depends on the observer state $\mathbf{x}_{o,i}$, the observer orientation and angular velocity $\boldsymbol{\theta}_{\mathcal{N}}^{\mathcal{O}_i}$ and $\boldsymbol{\omega}_{\mathcal{N}}^{\mathcal{O}_i}$, the i^{th} RSO state $\mathbf{x}_i$, the integration time t_I, and any number of EOS, RSO, and environmental parameters $\mathbf{d}_i \in \mathbb{R}^d$, $\mathbf{p}_j \in \mathcal{P} \subseteq \mathbb{R}^r$, and $\mathbf{e}_{ij} \in \mathcal{E} \subseteq \mathbb{R}^v$, respectively. Notationally, this relationship may be expressed as $p_{ij,d}(\mathbf{x}_j; \mathbf{x}_{o,i}, t_I, \mathbf{d}_i, \mathbf{p}_j, t) \in [0, 1]$. With these fundamental constraints and detection probability relationships given, it is now possible to focus on the definition of a performance objective in the following section.

G. Constellation & Operations Design Objective

There are many of conceivable objectives for a constellation of passive observing CubeSats. Some possible objectives are the number of unique detections over a specified time period, the expected number of re-acquisitions (of all objects) per day, or simply the total number of observations. The authors believe that multiple objectives are appropriate for the problem, however it is the scope of future work to develop additional objectives using the analytical framework introduced here. As a note, such additional performance objective functions may be enforced as inequality constraints in a system design or a full Multi-Objective Optimization (MOO) approach may be pursued.

To define the scope of this effort, the performance objective is to maximize the number of unique space object detections over some time period T. A 'detection' here is defined as occurring when a space object $\mathbf{x}_j$ both satisfies the geometric constraints $\mathcal{D}_i$ for any observer i ($\mathbf{x}_j \in \mathcal{D}_i$) and a random draw P from the uniform interval $\mathcal{U}[0, 1]$ is greater than the probability of detection by observer i indicated in Eq. (32). While this objective does not prohibit subsequent space object detections by the same or other observers, it does not reward multiple detections either. The purpose of such an objective is to optimize the coverage of a CubeSat constellation. A separate variation of the time interval over which unique detections are considered can address information timeliness requirements. It should be emphasized that the proposed objective is simply one of many possible objectives, and that the mathematical derivation of the analytic form of this objective may be adjusted for other objectives of interest.

From an optimization perspective, the decision variables considered here are the number of

constellation CubeSats N, each of which necessitate the optimization of the observer states $\mathbf{x}_{o,i}(t)$ and EOS attitude trajectory $(\boldsymbol{\theta}_{\mathcal{N}}^{\mathcal{O}_i}(t), \boldsymbol{\omega}_{\mathcal{N}}^{\mathcal{O}_i}(t))$ over the time interval $t \in [0, T]$, EOS integration time t_I, EOS cadence t_C, and observer design parameters $\mathbf{d}_i$. The RSO parameters $\mathbf{p}_j$ and environmental parameters $\mathbf{e}_{ij}$ are considered either random or given, and are not considered design parameters. The observer design parameters $\mathbf{p}_i$ may include any and all pertinent design parameters from focal length to actuator capabilities.

To properly motivate any rigorous discussion on maximizing the number of detected space objects, an *a-priori* assumption on the probability density function (PDF) of RSOs on orbit must be made. Such a proposition is fundamentally problematic given the problem at hand – the purpose of a proposed CubeSat constellation is to detect and characterize the RSO population, however to do so optimally requires some information regarding the character of the ostensibly undetected RSO population. However, the problem is not intractable. Two possible choices are to 1) use admissible region-like methods [63] to consider all closed orbits about Earth, or, more realistically, 2) use the SOC or the NASA ORDEM 3.0 model [64] to approximate the *a-priori* RSO density. Such a RSO PDF suggested by option 2) is written as $f(\mathbf{x}, t)$, $f : \mathbb{R}^6 \times T \to \mathbb{R}^+$, where by definition $\int_{\mathcal{X}} f(\mathbf{x}, t)\mathrm{d}\mathbf{x} = 1$ when $\mathcal{X}$ encapsulates the full state space.

Since the number of RSOs is necessarily an unknown number, the following analysis simply maximizes the fraction of unique detected objects represented by the PDF $f(\mathbf{x}, t)$. To begin the analytical derivation, first consider the conditional probability of observer i detecting at any instant an object j existing within $\mathcal{D}_i$ drawn from $f(\mathbf{x}, t)$.

$$\mathbb{P}\left[\text{detection}(\mathbf{x}_j)\right] = \mathbb{P}\left[(\mathbf{X}_j \sim f(\mathbf{x}, t)) \cap (\mathbf{X}_j \in \mathcal{D}_i) \cap (p_{ij,d} \geq P \sim \mathcal{U}[0, 1])\right] \tag{38}$$

Using Bayes' rule, Eqn. (38) may be used to compute the fraction F_i of existing objects detectable at time t by EOS i:

$$\mathbb{P}\left[\text{detection}\right] = \frac{\mathbb{P}\left[\text{detection}|\mathbf{X} \in \mathcal{D}_i\right]\mathbb{P}\left[\mathbf{X} \in \mathcal{D}_i\right]}{\mathbb{P}\left[\mathbf{X} \in \mathcal{D}_i|\text{detection}\right]} \tag{39}$$

$$\to F_i(t; \mathbf{z}(t)) = \int_{\mathcal{D}_i} p_{ij,d}(\mathbf{x}; \mathbf{z}, \cdot, t) f(\mathbf{x}, t)\mathrm{d}\mathbf{x} \tag{40}$$

The decision variable $\mathbf{z}(t)$ is used to encompass all decision variables $\mathbf{x}_{o,i}(t)$, $(\boldsymbol{\theta}_{\mathcal{N}}^{\mathcal{O}_i}(t), \boldsymbol{\omega}_{\mathcal{N}}^{\mathcal{O}_i}(t))$, t_I, and $\mathbf{d}_i$ previously identified. Additionally, $f(\mathbf{x}, t)$ must be computed for all $t \in T$ using the Fokker-Planck partial differential equation. To compute the number of unique detections made by EOS i over the time interval T, it is necessary to consider the volume of detectable state space over all possible instants in T, notationally written as $\mathcal{D}_i \times T \subseteq \mathcal{X} \times T$. When there are N such EOS observers, to avoid duplicate detections the set union operator may be used, defining the total set

of geometrically detectable states and times for the entire constellation.

$$\Omega = \mathcal{D} \times T \equiv \bigcup_{i=1}^{N} (\mathcal{D}_i \times T) \tag{41}$$

Then, the fraction of all RSOs detected by a constellation of N CubeSats may be expressed as

$$F_N(\mathbf{z}, T) = \int_{\Omega} p_{ij,d}(\mathbf{x}; \mathbf{z}, \cdot, t) f(\mathbf{x}, t) \mathrm{d}\Omega \tag{42}$$

Here, $F(\mathbf{z}, T) \in [0, 1]$ is computed assuming a specific set of RSO parameters $\mathbf{p}_i$ and environmental parameters $\mathbf{e}_{ij}$ $\forall i, j$. These parameters are not necessarily the same for each of the unknown number of RSOs, so each point $\mathbf{x} \in \mathcal{X}$ in the integrand of Eq. (42) may have RSO properties $\mathbf{p}$ and environmental parameters $\mathbf{e}$ drawn from an appropriately defined random distribution with PDF $\tilde{f}(\mathbf{p}, \mathbf{x}, t)$, with $\tilde{f} : \mathbb{R}^6 \times \mathcal{P} \times \mathcal{E} \times T \to \mathbb{R}^+$ capturing any joint dependence of the random variables. If this is the case, the domain of consideration Ω must be modified to include all permutations of the RSO and environmental parameters. With this consideration, the modified domain $\tilde{\Omega}$ is given as

$$\tilde{\Omega} = \mathcal{D} \times \mathcal{P} \times \mathcal{E} \times T \equiv \bigcup_{i=1}^{N} (\mathcal{D}_i \times \mathcal{P} \times \mathcal{E} \times T) \tag{43}$$

which allows the fraction of all RSOs detected by the constellation for all RSO parameters and environmental conditions to be computed as

$$\tilde{F}_N(\mathbf{z}, T) = \int_{\tilde{\Omega}} p_{ij,d}(\mathbf{x}; \mathbf{z}, \mathbf{p}, \mathbf{e}, t) \tilde{f}(\mathbf{x}, \mathbf{p}, \mathbf{e}, t) \mathrm{d}\tilde{\Omega} \tag{44}$$

The constellation and CONOPS design problem may be written as an optimization problem with the objective function Eq. (42) as follows

Problem 1 (Space Situational Awareness Constellation Optimization)**.** *Determining an SSA constellation of passive EOS sensors (ground-based, space-based, or both) that maximizes the unique detections over a time interval T is equivalent to the following optimization problem:*

$$\begin{aligned} \min_{N,\boldsymbol{z}} \; & J(N, \boldsymbol{z}, T) = -\tilde{F}_N(\boldsymbol{z}, T) \\ \textit{subject to: } & \dot{\boldsymbol{z}} = \boldsymbol{f}_z(\boldsymbol{z}, t),\ t \in T \\ & \boldsymbol{z} \in \left(\mathcal{X} \times \mathrm{SO}(3) \times \mathbb{R}^3 \times \mathcal{P}\right) \times N \\ & N \in \mathbb{N} \end{aligned}$$

where N is the number of spacecraft, $\boldsymbol{f}_z : \mathbb{R} \times T \to \mathbb{R}$ captures any dynamics of the inertial state, orientation states, and parameters for all N spacecraft, $\mathcal{Z} \equiv (\mathcal{X} \times \mathrm{SO}(3) \times \mathbb{R}^3 \times \mathcal{P}) \times N$

defines the set of admissible decision parameters for all N spacecraft, and $\mathbb{N}$ is the set of natural numbers. The decision variable $\boldsymbol{z}$ is composed of inertial observer states $\boldsymbol{x}_{o,i}$, orientation states $(\boldsymbol{\theta}_{\mathcal{N}}^{\mathcal{O}_i}(t), \boldsymbol{\omega}_{\mathcal{N}}^{\mathcal{O}_i}(t))$, spacecraft design parameters $\boldsymbol{d}_i$ $\forall i = 1, \ldots, N$.

Emphatically, the single-objective performance optimization articulated in Problem 1 has nonlinear time-varying states, potentially possesses discrete design parameters within $\mathbf{d}_i$, and has an integer number of spacecraft N. Hence, even the 'simplified' formulation in Problem 1 is inherently a mixed integer nonlinear programming problem (MINLP). Such problems suffer from both nonlinear programming (NLP) and mixed integer (MI) drawbacks. Problem 1 in particular is nonconvex, suffers from a surfeit of local minima, and possesses a relatively large number of variables. Further, the dimension of the statespace increases linearly with the number of spacecraft. From a mixed integer perspective, the number of constellation spacecraft N and possible discrete states within each $\mathbf{p}_i$ mean that the computational complexity of the problem increases exponentially with the number of discrete states (which is always at least one) Thus, Problem 1 is NP-complete, and appears to be computationally intractable (even if the decision space were convex, it would still be NP-hard) [65]. The following section discusses several high level relaxations made to form a tractable problem for the analysis contained within this paper.

H. Approximate Solution Approach

To reduce the MINLP identified in Problem 1 to a computationally tractable problem, the approach taken here is to choose the majority of decision variables based on a combination of logic, design experience, and hardware availability. Then, remaining decision variables are optimized using numerical methods. While this solution approach is clearly not optimal and contains a number of ad-hoc assumptions, it is hoped that this first attempt to solve Problem 1 serves as a starting point for future efforts.

The general outline for this strategy is given here. In §VI.I, the attitude trajectory for each observer EOS i is chosen, largely defining the CONOPS design used in this paper. In §VII, assorted spacecraft and EOS design parameters are chosen based on a combination of analysis and ranking of available commercial off-the-shelf (COTS) components. Additionally, the computational complexity of necessary algorithms and their impact on operational EOS cadence is also discussed. Finally, in §II, the problem is further reduced to a more traditional constellation design problem wherein the satellites are distributed over circular orbits parameterized by a Walker constellation. In the final optimization problem, the remaining decision variables include only the number of constellation satellites, number of orbit planes, the semi-major axis, and the inclination of each orbit plane. Additionally, because the constellation performance with respect to Eqn. (44) nominally improves as N becomes larger, the cost of the constellation is also modeled in §II to provide an additional objective function that naturally forms a Pareto frontier with the performance objective in Eqn. (44). Table 6 gives an extensive list of all of the parameters and decision variables for the

final optimization problem used in this paper to generate the Pareto frontier.

Table 6. All decision variables, z

Parameter	Symbol	Determined in
CONOPS Variables:		
Translational States	$\left(\mathbf{o}_i^T(t),\ \dot{\mathbf{o}}_i^T(t)\right)$	§VI.A and §III.A
Rotational States	$\left(\boldsymbol{\theta}_{\mathcal{N}}^{\mathcal{O}_i}(t),\ \boldsymbol{\omega}_{\mathcal{N}}^{\mathcal{O}_i}(t)\right)$	§VI.F and §III.A
Payload Parameters, $\mathbf{d}_i$:		
Signal to Noise Ratio	SNR_{alg}	§VII.C.2
Pixels occupied by RSO	$m_{ij,0}$	§VII.C.2
Focal length	l	§VII.C.1
F-number	ν	§VII.C.1
Aperture diameter	D	§VII.C.1
Horizontal FOV	FOV_h	§VII.C.2
Vertical FOV	FOV_v	§VII.C.2
Pixel size	p	§VII.C.2
Sensor resolution	$n_{p,h} \times n_{p,v}$	§VII.C.2
Quantum Efficiency	QE	§VII.C.2
Optical transmittance	τ_{opt}	§VII.C.2
Dark current per pixel	$q_{\text{p,dark}}$	§VII.C.2
Cadence Time	t_C	§VII.C.3
Integration Time	t_I	§VII.C.3
Environmental Parameters, $\mathbf{e}_{ij}$:		
Background radiant intensity	$q_{\text{p,bkg}}$	§VII.C.2
Spectral excitement of a mag. 0 object	Φ_0	§VII.C.2
Atmospheric transmittance	τ_{atm}	§VII.C.2
Relative angular rate	$\dot{\eta}_{ij}$	§VII.C.2
Constellation Parameters:		
Number of Satellites	N	Decision Variable: §III.A
Number of Planes	P	Decision Variable: §III.A
Semi-Major Axis	a	Decision Variable: §III.A
Inclination	i	Decision Variable: §III.A

I. CONOPS Design

To design an attitude trajectory through the rotation group $\text{SO}(3)$ for each observer EOS, i, it is helpful to first revisit the principal geometric constraints satisfied as preconditions to each detection. Namely, a RSO must be 1) within line-of-sight, 2) within the field of view, and 3) illuminated. Naturally, one may assume that to detect the largest number of RSOs, the EOS should be oriented towards regions of illuminated space that do not have the Earth, moon, or sun in the background and are relatively dense with debris. Just such a set of locations are the volumes of space above the north and south poles. Both regions possess the largest spatial density of space objects [64],

and also have large fractions of the debris fields from recent on-orbit collisions and explosions. Conversely, very few spacecraft have been launched in to extremely low inclinations (below 20 degrees, for example), so there is little incentive to search for space debris in the volume of space near the equator. Lastly, the majority of debris is in LEO, so an attitude trajectory consistent with detecting high inclination LEO objects is preferable given the objective in Eqn. (44).

If the constellation is concerned with detecting LEO space objects, the EOS sensors should be placed in or near LEO to maximize the number of detections (recall that reflected / emitted photon flux collected by EOS i drops off as $1/\rho_{ij}^2$). With these facts in mind, it is determined here that periodic attitude trajectories wherein each EOS i observes volumes at or near the north and south poles provides the largest quantity of unique detections. Therefore, the attitude trajectory is chosen as follows:

1. EOS i should align its FOV towards geosynchronous orbit altitudes once it is within 5 degrees of its ascending node. The FOV should be aligned with the zenith direction at the ascending node.

2. Pointing at this volume of space should continue until EOS i is more than 5 degrees from its ascending node.

3. After passing more than 5 degrees from the ascending node, EOS i should align its FOV towards the volume of space above the north pole with the highest spatial density of RSOs and the smallest possible solar phase angle ϕ_i to a point within the volume (if it satisfies the LoS constraint).

4. Pointing at this volume of space should continue until the LoS constraint is no longer satisfied, or until the descending node is within 5 degrees.

5. EOS i should align its FOV towards geosynchronous orbit altitudes once it is within 5 degrees of its descending node. The FOV should be aligned with the zenith direction at the descending node.

6. Pointing at this volume of space should continue until EOS i is more than 5 degrees from its descending node.

7. After passing more than 5 degrees from the descending node, EOS i should align its FOV towards the volume of space above the south pole with the highest spatial density of RSOs and the smallest possible solar phase angle ϕ_i to a point within the volume (if it satisfies the LoS constraint).

8. Pointing at this volume of space should continue until the LoS constraint is no longer satisfied, or until the ascending node is within 5 degrees.

The simple EOS attitude trajectory defined by this cyclical CONOPS is used for the remainder of this paper. There are many areas of improvement that may be considered, particularly if additional objective functions are defined. For example, an operator may not care only about the number of unique detections, but potentially the frequency of detections or detections for underrepresented populations in existing catalogs or statistical models [64]. If this is the case, then clearly the CONOPS defined here should be revisited.

VII. Parametric CubeSat Design

This section introduces the parameters involved in the design of an EOS for a CubeSat mission. Each of these parameters are informed by the CONOPS and directly impact the performance of the CubeSat mission. As described in §VI.H, this section constrains the optimization problem defined in Problem 1 by defining the spacecraft parameters $\mathbf{d}_i$.

A. Telescope Scaling

SSA mission architectures dictate a need to detect as many objects as possible, detect the dimmest objects possible, and obtain detections with as much accuracy as possible, providing criteria by which the system's optical sensor can be sized. While many parameters affect the performance of an optical sensor, aperture diameter D, pixel size p, and focal length l are the most dominant parameters used to quantify the performance of a given optical system [61]. Integration time may be used in conjunction with these optical parameters to determine the cadence of image acquisition for the system to detect objects of a given magnitude. An analysis on these sizing parameters can be used to narrow prospective optics choices, but is not considered an absolute means to obtain a final system design.

By using the three parameters stated above, the IFOV for a given optical system can be defined, where ν refers to f-number, a commonly used parameter for describing optical systems.

$$\nu = l/D \tag{45}$$

$$\text{IFOV} = 2\text{arctan}\left(\frac{p}{2\nu D}\right) \tag{46}$$

IFOV can be described as the FOV for a single pixel. This parameter is important in determining the overall FOV for an optical sensor, as well as determining the accuracy of a system. The following equation shows how to calculate the vertical and horizontal components of FOV, FOV_v and FOV_h respectively, where n_p is the number of pixels in a given sensor in each direction.

$$\text{FOV}_v = n_{p,v}\text{IFOV} \tag{47}$$

$$\text{FOV}_h = n_{p,h}\text{IFOV} \tag{48}$$

Optical systems with larger FOVs can view larger areas and thus are capable of detecting a larger volume of objects, N_C, per frame; however, because a sensor with a larger IFOV is capturing photons from a larger area, the precise location of any detected object is less accurately defined. As a result, a tradeoff must be made between detection of more objects, which is achieved with a higher FOV, and accuracy of detections, which is achieved with a lower IFOV, which in turn affect all three of the design parameters, D, l, and p. The impact of this tradeoff can be mitigated by choosing a sensor with a higher number of pixels, but consideration then needs to be given to other aspects of the sensor design such as power draw, physical dimensions, and computational requirements. Additionally, a higher FOV sensor is capable of detecting objects with higher relative angular velocities [66].

To quantify the limiting magnitude, or dimmest signature observable by an optical system, a metric for limiting magnitude needs to be defined. In the below equation, m_v is the limiting magnitude.

$$m_v = -2.5\log_{10}\left[\frac{\text{SNR}_{i,\text{alg}}\left[\sqrt{m_{ij}}\dot{\eta}_{ij}\nu D(q_{i,\text{p,bkg}} + q_{i,\text{p,dark}})\right]^{\frac{1}{2}}}{\Phi_0 \tau_{\text{atm}} \tau_{\text{opt}} (\frac{\pi D^2}{4}) \text{QE} \sqrt{p}}\right] \tag{49}$$

The above equation, developed by Coder and Holzinger [61], incorporates a minimum detectable signal to noise ratio (SNR), which is defined as the ratio of photons emitted by the target object to the photons emitted by all other noise sources. m_{ij} is the number of pixels occupied by photons from RSO j as seen by EOS i, $\dot{\eta}_{ij}$ is the apparent angular rate between the sensor motion and the space object, $q_{i,\text{p,bkg}}$ is background radiant intensity per pixel, $q_{i,\text{p,dark}}$ is dark current per pixel, Φ_0 is the spectral excitement of a magnitude 0 object , τ_{atm} is atmospheric transmittance, τ_{opt} is optical transmittance, and QE is the quantum efficiency of a given sensor. Again, a higher limiting magnitude indicates that dimmer objects can be detected, so it is desirable to maximize this value. In terms of design parameters, this implies a longer focal length l, and lower aperture diameter, D.

B. Image Processing Scaling

Image processing can be divided into object detection and object tracking. Detection can be accomplished through use of blob-detection algorithms, of which many implementations are available through open source software packages[c] [d].

Many algorithms exist for the purpose of tracking objects within a set of sequential images, ranging from simple nearest-neighbor approaches to more computationally intensive multi-target multiple hypothesis tracking (MHT) algorithms [67]. Such MHT codes tend to be exceptionally robust, but because the number of possible object tracks grows exponentially, this can quickly create an unwieldy problem for a CubeSat processor, making real-time implementation difficult.

[c] via www.opencv.org; accessed 6/1/2015

[d] via www.v3ga.net/processing/BlobDetection; accessed 6/1/2015

By paring down the number of possible track assignments to some k-best number of tracks, the k-best MHT algorithm can reach speeds 100 times faster than traditional MHT, allowing k-best MHT to become acceptable for real-time cubesat missions [68]. For analysis purposes, we state that the processing speed of a k-best MHT algorithm is $\mathcal{O}(n^c)$, where c is the number of images between track pruning. In practice, c can be set to 2, meaning possible tracks are calculated for all objects in two subsequent images, then pruned back to the k best tracks between images. This allows order of magnitude analysis for run times and later image cadence.

C. Parametric Design for CubeSats

When choosing a CubeSat architecture for an SSA mission, preference is placed on a larger form factor to accommodate larger optics. There is, however, a limit on the size of commercially available CubeSat structures. A 6U CubeSat structure is chosen in this analysis because it is one of the largest CubeSat structures readily available off-the-shelf. Selection of a passive optical payload system is broken into discussions of aperture diameter, sensor selection, focal length, and cadence in order to discretize the design problem.

1. Aperture Diameter

Given a 6U CubeSat structural architecture, the two largest aperture diameter lenses allowed are 10cm (1U) on the smaller faces and 20cm (2U) on the largest faces as illustrated in Figure 13. While both 1U and 2U diameter aperture options are physically possible on a 6U CubeSat, each

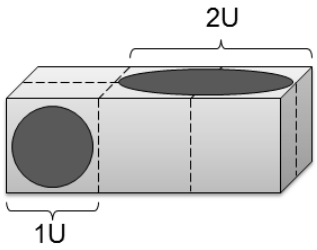

Figure 13. 1U and 2U aperture design options for a 6U CubeSat.

case involves additional constraints. Because lenses with 20cm diameters and multiple mirrors are not available off-the-shelf, the focal length of a 2U diameter lens's optical system could be at maximum 10cm, requiring an f-number of less than 0.5. If such optical trains become available in the future, the 2U diameter aperture case could be revisited as an attractive alternative, but is not considered in this analysis. The 1U diameter aperture case allows a focal length of up to 30cm, or an f-number of less than 3. Secondary mirrors are ruled out of the 1U case because with increasing f-number, FOV decreases which results in fewer object detections. Because of the availability of commercial-off-the-shelf (COTS) lens options which satisfy the 1U aperture requirement, this paper focuses on the 1U case. A sample of COTS lens components that fit within the 1U diameter

limit, outlined in Table 7, are examined to find a suitable component within the design space. Tables 7 and 8 also include a summary of the values used for calculating the utopia points in Figures 14 and 15, discussed in §VII.C.2.

Table 7. Sample COTS Lens components

Lens	Focal length (mm)	F-Number, ν	Aperture diameter, D (mm)
ThorLabs MVL50HS [e]	50	0.95	52.6
Kowa LM60JS5MA [f]	60	0.8	75.0
Lensagon CM5014GS [g]	50	1.4	35.7
Edmund Optics [h]	75	1.8	41.7
Utopia point	300	3	100

Camera to lens connection mounts are standardized in industry, meaning that if a camera and lens have differing mounts an adapter can be found to make the components compatible. For this reason, lenses and cameras can be examined separately without paying special consideration to the type of mount. Also, as seen in the table above, the Kowa LM60 lens has a significantly larger maximum aperture diameter compared with the other sample lenses. While this provides an advantage in the amount of light the lens can collect, a decision cannot be made until all possible sensor and lens combinations are examined to determine the system's IFOV, FOV, and limiting magnitude.

2. *Sensor Selection*

Again, a sample of COTS components capable of working in a 1U constraint, not considering the camera's axial direction, are examined as seen in Table 8.

Table 8. Sample COTS sensor components

Sensor	Pixel size (μm)	Resolution ($n_{p,h} \times n_{p,v}$)	Quantum Efficiency
Photonis Nocturn XL [i]	9.7	1280×1024	0.60
Pointe Grey Flea3 GE-14S3M-C [j]	4.65	1384×1032	0.53
Toshiba IK-HR1H [k]	5	1920×1080	0.60
Gomspace NanoCam C1U [l]	3.2	2048×1536	0.36
Utopia point	10	10000×10000	1.00

[e] via www.thorlabs.com; accessed 6/1/2015
[f] via www.kowa.eu; accessed 6/1/2015
[g] via www.lensation.de; accessed 6/1/2015
[h] via www.edmundoptics.com; accessed 6/1/2015
[i] via www.photonis.com; accessed 6/1/2015
[j] via www.ptgrey.com; accessed 6/1/2015
[k] via www.toshibacameras.com; accessed 6/1/2015
[l] via gomspace.com; accessed 6/1/2015

To evaluate the possible combinations of sensor and lens, limiting magnitude, IFOV, and FOV are computed, utilizing the values shown in Table 9 along with values for each sensor and lens shown in Tables 7 and 8, with results plotted in Figures 14 and 15. Here, $\mathbb{E}\left[\dot{\eta}_{ij}\right]$ is an average value for all $\dot{\eta}_{ij}$ selected for the express purpose of evaluating the point design considered here. In the results and simulation, §III.A, this value is computed using the true observer and RSO locations.

Table 9. Payload evaluation parameters

Parameter	Units	Value
SNR_{alg}	—	4
m_i	pixels	1
$\mathbb{E}\left[\dot{\eta}_{ij}\right]$	rad/s	0.0056
$q_{\text{p,bkg}}$	m_v/as^2	0.0364
$q_{\text{p,dark}}$	e/pixel/s	0.5
Φ_0	photons/s/m^2	5.6×10^{10}
τ_{atm}	—	1
τ_{opt}	—	0.9

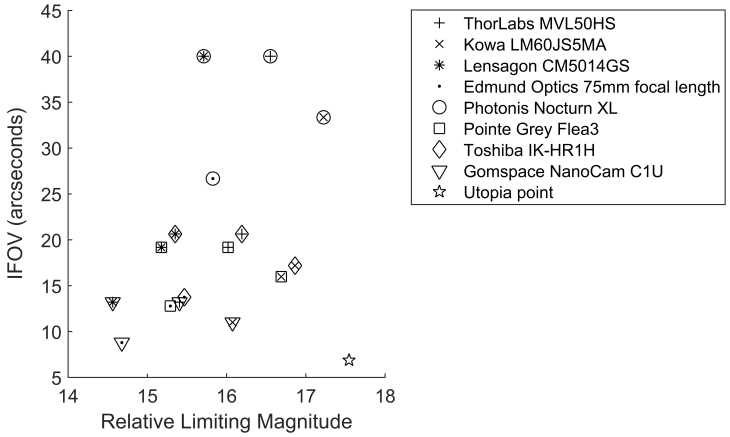

Figure 14. Relative limiting magnitude versus IFOV of all sample lens and sensor combinations. For each point, interior marks describe lens options, and exterior marks describe sensor options.

In order to evaluate possible lens and sensor options, it is useful to define an optimum, or utopia point for the system's performance. For this system, it is not possible to maximize all design goals due to conflicting optimum design goal parameters, so the following method was used to set the utopia points. Utopia points are created by setting aperture diameter D to 10cm, Quantum Efficiency to 1, sensor resolution to 10,000 by 10,000, pixel size p to 10μm, and f-number ν to 3, with all other evaluation parameters fixed as listed in Table 9. These values were calculated by assuming the best case payload would maximize both aperture diameter and sensor size. To that end, the maximum aperture diameter D for the 1U case fills the entire 10cm face. Focal

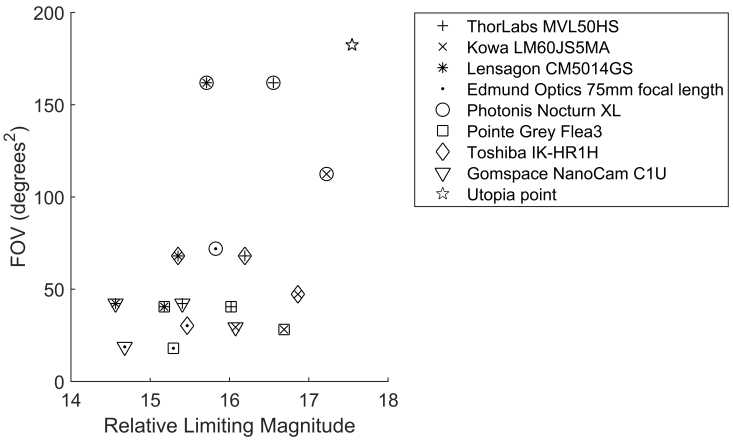

Figure 15. Relative limiting magnitude versus FOV of all sample lens and sensor combinations. For each point, interior marks describe lens options, and exterior marks describe sensor options.

length is also maximized to 300mm, the maximum along the 3U face of the CubeSt, and Quantum Efficiency is maximized to 1. F-number falls out of the values assigned to aperture diameter D and focal length l. The sensor is maximized to fill the 100mm $\times$ 100mm area, requiring a tradeoff between pixel size p and sensor resolution $n_{p,h}\times\ n_{p,v}$, as shown in Equation (50). Neither n_p nor p can be maximized because this results in either one large pixel which would render objects indistinguishable, or infinite pixels which cannot be used for calculations. Therefore a point is selected which is believed to be a reasonable midpoint between the two, giving $n_{p,h}\times\ n_{p,v}$ equal to 10000 $\times$ 10000 and p equal to 10μm, which results in the maximum sensor size of 100 $\times$ 100 mm.

$$\left\{ \begin{array}{c} n_{p,h} \times p \\ n_{p,v} \times p \end{array} \right\} = 100\text{mm} \tag{50}$$

By examining the utopia points in Figures 14 and 15, it is apparent that IFOV and FOV require conflicting parameter ideals for optical train performance. The optical system that lies closest to both utopia points, the Kowa LM60JS5MA lens with the Photonis Nocturn XL, is selected for further analysis. The specifications of this system are summarized in Table 10.

Table 10. Summary of Selected Payload parameters

Parameter	Units	Value
Focal length l	mm	60.0
F-number ν	—	0.80
Aperture diameter D	mm	75.0
Pixel size p	μm	9.70
Sensor resolution ($n_{p,h} \times n_{p,v}$)	pixels	1280×1024
Quantum Efficiency	—	0.60

3. *Focal length and Cadence*

The cadence, t_C, may be defined as the sum of integration time, t_I, image transfer time, t_t, and image processing time, t_p. Two cases may be defined, however, where image processing time and image integration time overlap, as seen in Equation (51).

$$t_C = \begin{cases} t_I + t_t \text{ if } t_I \geq t_p \\ t_t + t_p \text{ if } t_I < t_p \end{cases} \tag{51}$$

Taking a constant integration time of 33 milliseconds, a base processing time of 0.0175 seconds per object detected, nominal tracking of 300 objects per image, and a nominal object density of 5 objects per degree squared, it can be seen in Figure 3 that image cadence is dominated by image processing speed. This base processing time per object detected is based on lab work done for the RECONSO CubeSat at Georgia Tech using a BeagleBone processor. Processing times will vary depending on the processor and algorithms selected for each mission. Object density per square degree is estimated by summing the total number of objects in JSpOC's SOC with the total number of stars in the Hipparcos star catalog, and dividing by the total solid angles in degrees squared of a sphere. While the Hipparcos star catalog contains entries down to magnitude 14, it is not considered a complete record. An approximately 50 percent margin is therefor added to this value to account for objects not listed in either catalog. In practice, a threshold can be placed for the maximum number of stars to be tracked to decrease processing time further.

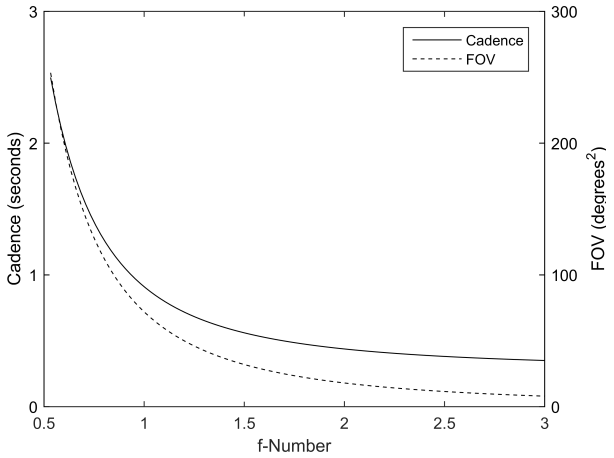

Figure 16. Image cadence in seconds between images, and FOV with respect to f-number

To choose a cadence for a given mission design, a trade-off must be made between cadence and FOV, or detectable objects. Further analysis may be performed to determine the maximum acceptable time between images based on the relative velocities of RSOs to be tracked, such that objects will remain in the FOV between subsequent frames, which will allow RSO trajectories to be tracked. In summary, Figure 3 shows that there is a diminishing return in cadence for higher

f-numbers as well as a sharp rise in the required time between images at lower f-numbers. Figure 3 also shows that FOV rises with lower f-numbers and decreases slowly with higher f-numbers.

References

[1] D. O. Whitlock, "History of on-orbit satellite fragmentations," 13th edition, Lyndon B. Johnson Space Center, 2004.

[2] E. P. Chatters and B. J. Crothers, "Space Surveillance Network," *Air University Space Primer*, US Air Force, 2009, Ch.19, pp. 249–258.

[3] D. Shoots, "International space station performs fourth and fifth debris avoidance maneuvers of 2014," Vol. 19(1) Orbital Debris Quarterly, NASA Orbital Debris Program Office, 2015.

[4] M. Morton and T. Roberts, "Joint Space Operations Center (JSpOC) Mission System (JMS)," *AMOS Technologies Conference, Maui, HI*, 2011.

[5] G. Gleghorn, "Orbital debris: A Technical assessment," Committee on Space Debris, National Research Council, National Academy Press, 1995.

[6] W. Bauer, O. Romberg, C. Wiedemann, G. Drolshagen, and P. Vörsmann, "Development of in-situ Space Debris Detector," *Advances in Space Research*, Vol. 54, No. 9, 2014, pp. 1858–1869, DOI: 10.1016/j.asr.2014.07.035.

[7] D. S. McKnight and F. R. Di Pentino, "New insights on the orbital debris collision hazard at GEO," *Acta Astronautica*, Vol. 85, 2013, pp. 73–82, DOI: 10.1016/j.actaastro.2012.12.006.

[8] S. Kan, "China's Anti-Satellite Weapon Test," report, Congressional Research Service, Library of Congress order code RS22652, 2007.

[9] T. Wang, "Analysis of Debris from the Collision of the Cosmos 2251 and the Iridium 33 Satellites," *Science and Global Security*, Vol. 18, No. 2, 2010, pp. 87–118, DOI: 10.1080/08929882.2010.493078.

[10] T. S. Kelso, "Analysis of the Iridium 33-Cosmos 2251 collision," *Astrodynamics*, Vol. 135(1-3), 2010, pp. 1099–1112.

[11] C. Murray, "China Missile Launch May Have Tested Part of a New Anti-Satellite Capability," US Congress, US-China Economic and Security Review Commision, 2013.

[12] D. J. Heimerdinger, "Orbital Debris and Associated Space Flight Risks," *Reliability and Maintainability Symposium*, Alexandria, VA, IEEE, 2005, DOI: 10.1109/RAMS.2005.1408413.

[13] D. Shoots, "Update on 3 Major Debris Clouds," Vol. 14(2) Orbital Debris Quarterly, NASA Orbital Debris Program Program Office, 2010.

[14] E. Christiansen, J. Hyde, and R. Bernhard, "Space Shuttle debris and meteoroid impacts," *Advances in Space Research*, Vol. 34, No. 5, 2004, pp. 1097–1103, DOI: 10.1016/j.asr.2003.12.008.

[15] D. J. Kessler and B. G. Cour-Palais, "Collision Frequency of Artificial Satellites: The Creation of a Debris Belt," *Journal of Geophysical Research*, Vol. 83, No. A6, 1978, pp. 2637–2646, DOI: 10.1029/JA083iA06p02637.

[16] "National Space Policy of the United States of America," Office of the President of the United States, Washington, D.C., 2010.

[17] C. M. Scaparotti, "Joint Publication 3-14, Space Operations," US Department of Defense, Joint Chiefs of Staff, Washington, D.C., 2013.

[18] "Technology Horizons," Vol. 1, Office of the US Air Force Chief Scientist, Library of Congress, 2011, ISBN: AF/ST-TR-10-01-PR.

[19] R. F. Hale, "United States Department Of Defense Fiscal Year 2016 Budget Request," Department of Defense, Office of the Under Secretary of Defense, Chief Financial Officer, 2015.

[20] "Report of the Scientific and Technical Subcommittee on its fifty-second session," Vol. 10(19), United Nations, Committee on the Peaceful Uses of Outer Space, 2015, ISBN: A/AC.105/1088.

[21] A. E. Potter, *Ground-based optical observations of orbital debris - a review*, Vol. 16 of *Advances in Space Research*, pp. 35–45. Pergamon Press Ltd, 1995, DOI: 10.1016/0273-1177(95)98751-9.

[22] A. A. Grometstein, "MIT Lincoln Laboratory Technology in Support of National Security," Lexington, MA, Lincoln Laboratory, 2011, ISBN: 978-0-615-42880-2.

[23] J. L. Foster, J. R. Benbrook, and E. G. Stansbery, *Detection of small radar cross-section orbital debris with the Haystack radar*, Vol. 35 of *Advances in Space Research*, pp. 1210–1213. Kidlington: Pergamon Press Ltd, 2005, DOI: 10.1016/j.asr.2005.05.041.

[24] T. W. Thompson, R. M. Goldstein, D. B. Campbell, E. G. Stansbery, and A. E. Potter, "Radar detection of centimeter-sized orbital debris - preliminary arecibo observations at 12.5-cm wavelength," *Geophysical Research Letters*, Vol. 19, No. 3, 1992, pp. 257–259, DOI: 10.1029/91gl02772.

[25] M. Gruntman, "Passive optical detection of submillimeter and millimeter size space debris in low Earth orbit," *Acta Astronautica*, Vol. 105, No. 1, 2014, pp. 156–170, DOI: 10.1016/j.actaastro.2014.08.022.

[26] W. Flury, A. Massart, T. Schildknecht, U. Hugentobler, J. Kuusela, and Z. Sodnik, "Searching for Small Debris in the Geostationary Ring," *ESA Bulletin*, Vol. 104, 2000.

[27] D. Monet, T. Axelrod, C. Claver, T. Blake, R. Lupton, E. Pearce, R. Shah, and D. Woods, "Rapid Cadence Collections with the Space Surveillance Telescope," US Naval Observatory Flagstaff Station, 2012.

[28] K. Malek, T. Batsch, M. Cwiok, W. Dominik, G. Kasprowicz, A. Majcher, A. Majczyna, L. Mankiewicz, K. Nawrocki, R. Pietrzak, L. W. Piotrowski, M. Ptasinska, M. Siudek, M. Sokolowski, J. Uzycki, P. Wawer, R. Wawrzaszek, G. Wrochna, M. Zaremba, and A. F. Zarnecki, "General overview of the 'Pi of the Sky' system," *Photonics Applications in Astronomy, Communications, Industry, and High-Energy Physics Experiments*, Vol. 7502, 2009, DOI: 10.1117/12.837741.

[29] R. Wawrzaszek, P. Wawer, M. Sokolowski, K. Nawrocki, R. Pietrzak, K. Malek, M. Zaremba, and L. W. Piotrowski, "Possible use of the 'Pi of the Sky' system in a Space Situational Awareness program," *Photonics Applications in Astronomy, Communications, Industry, and High-Energy Physics Experiments*, Vol. 7502, 2009.

[30] G. Beskin, S. Bondar, S. Karpov, V. Plokhotnichenko, A. Guarnieri, C. Bartolini, G. Greco, A. Piccioni, and A. Shearer, "From TORTORA to MegaTORTORA—Results and Prospects of Search for Fast Optical Transients," *Advances in Astronomy*, Vol. 2010, 2010, DOI: 10.1155/2010/171569.

[31] D. Pollacco, I. Skillen, A. Cameron, D. Christian, C. Hellier, J. Irwin, T. Lister, R. Street, R. West, D. Anderson, W. Clarkson, H. Deeg, B. Enoch, A. Evans, A. Fitzsimmons, C. Haswell, S. Hodgkin, K. Horne, S. Kane, F. Keenan, P. Maxted, A. Norton, J. Osborne, N. Parley, R. Ryans, B. Smalley, P. Wheatley, and D. Wilson, "The WASP Project and the SuperWASP Cameras," *Publications of the Astronomical Society of the Pacific*, Vol. 118, 2006, pp. 1407–1418, DOI: 10.1086/508556.

[32] J. R. Shell, "Optimizing orbital debris monitoring with optical telescopes," AMOS Technologies Conference, Maui, HI, 2010.

[33] M. o. t. L. M. Group and D. S. Investigation, "Meteoroid and Debris Impact Features Documented on the Long Duration Exposure Facility," NASA, Lyndon B. Johnson Space Center, Publication 84, JSC 24608, 1990.

[34] J. C. Mandeville, C. R. Maag, and C. Durin, *In-situ detection of micrometeoroids and orbital debris: The PIE experiment on MIR*, Vol. 25 of *Advances in Space Research-Series*, pp. 329–334. Oxford: Pergamon Press Ltd, 2000, DOI: 10.1016/s0273-1177(99)00949-7.

[35] X. J. Fu, G. M. Liu, and M. G. Gao, "Overview of orbital debris detection using spaceborne radar," Iciea 2008: 3rd IEEE Conference on Industrial Electronics and Applications, Proceedings, Vols 1-3, New York, IEEE, 2008, pp. 1071–1074, ISBN: 978-1-4244-1718-6.

[36] M. E. Gaposchkin, C. von Braun, and J. Sharma, "Space-Based Space Surveillance with the Space-Based Visible," *Journal of Guidance Control and Dynamics*, Vol. 23, No. 1, 2000, pp. 148–152, DOI: 10.2514/2.4502.

[37] P. Maskell and L. Oram, "Sapphire: Canada's Answer to Space-Based Surveillance of Orbital Objects," AMOS Technologies Conference, Maui, HI, 2008.

[38] L. M. Simms, W. De Vries, V. Riot, S. S. Olivier, A. Pertica, B. J. Bauman, D. Phillion, and S. Nikolaev, "Space-based telescopes for actionable refinement of ephemeris pathfinder mission," *Optical Engineering*, Vol. 51, No. 1, 2012, p. 011004, DOI: 10.1117/1.OE.51.1.011004.

[39] R. F. Teehan, "Responsive Space Situation Awareness in 2020," US Air Force, Maxwell Air Force Base, 2007.

[40] J. Sharma, G. H. Stokes, C. von Braun, G. Zollinger, and A. J. Wiseman, "Toward Operational Space-Based Space Surveillance," *Lincoln Laboratory Journal*, Vol. 13, No. 2, 2002, pp. 309–334.

[41] L. M. Simms, V. Riot, W. De Vries, S. S. Olivier, A. Pertica, B. J. Bauman, D. Phillion, and S. Nikolaev, "Optical Payload for the STARE Mission," SPIE Defense and Security Conference, Orlando, FL, 2011.

[42] T. E. O'Brien, "Space Situational Awareness Cubesat Concept of Operations," Naval Postgraduate School, Masters Thesis, 2011.

[43] W. J. Larson and J. R. Wertz, "Space Mission Analysis and Design," 3rd edition, Space Technology Library, Microcosm, Ch. 19, 1999, ISBN: 978-1881883104.

[44] C. R. Boshuizen, J. Mason, P. Klupar, and S. Spanhake, "Results from the Planet Labs Flock Constellation," AIAA Conference on Small Satellites, Logan, UT, 2014.

[45] M. P. Ferringer, D. B. Spencer, P. M. Reed, R. S. Clifton, and T. G. Thompson, "Pareto-hypervolumes for the Reconfiguration of Satellite Constellations," AIAA/AAS Astrodynamics Specialist Conference and Exhibit, Honolulu, HI, 2008, DOI: 10.2514/6.2008-6611.

[46] T. A. Ely, W. A. Crossley, and E. A. Williams, "Satellite Constellation Design for Zonal Coverage Using Genetic Algorithms," *Journal of the Astronautical Sciences*, Vol. 47, No. 3 and 4, 1999, pp. 207–228.

[47] E. Frayssinhes, "Investigating new satellite constellation geometries with genetic algorithms," AIAA/AAS Astrodynamics Specialists Conference, San Diego, CA, 1996, pp. 582–586.

[48] W. J. Mason, V. Coverstone-Carroll, and J. W. Hartmann, "Optimal Earth Orbiting Satellite Constellations Via a Pareto Genetric Algorithm," 1998, DOI: 10.2514/6.1998-4381.

[49] H. Kiremitci, "Satellite Constellation Optimization for Turkish armed forces," Naval Postgraduate School, Masters Thesis, 2013.

[50] M. Hutchison, K. M. Kolarik, and J. Water, "Joint Space Operations Center (JSpOC) Mission System (JMS) Common Data Model: Foundation for Interoperable Data Sharing for Space Situational Awareness," The Aerospace Corporation, Ground System Architectures Workshop, Los Angeles, CA, 2013.

[51] J. G. Walker, "Circular orbit patterns providing continuous whole earth coverage," tech. rep., DTIC Document, 1970.

[52] D. C. Beste, "Design of satellite constellations for optimal continuous coverage," *Aerospace and Electronic Systems, IEEE Transactions on*, No. 3, 1978, pp. 466–473, DOI: 10.1109/TAES.1978.308608.

[53] A. Ballard, "Rosette constellations of earth satellites," *IEEE Transactions onAerospace and Electronic Systems*, No. 5, 1980, pp. 656–673, DOI: 10.1109/TAES.1980.308932.

[54] Y. P. Ulybyshev, "Design of satellite constellations with continuous coverage on elliptic orbits of Molniya type," *Cosmic Research*, Vol. 47, No. 4, 2009, pp. 310–321, DOI: 10.1134/S0010952509040066.

[55] J. E. Draim, "Three-and four-satellite continuous-coverage constellations," *Journal of Guidance, Control, and Dynamics*, Vol. 8, No. 6, 1985, pp. 725–730, DOI: 10.2514/3.20047.

[56] J. E. Draim, "A common-period four-satellite continuous global coverage constellation," *Journal of Guidance, Control, and Dynamics*, Vol. 10, No. 5, 1987, pp. 492–499, DOI: 10.2514/3.20244.

[57] D. Mortari and M. P. Wilkins, "Flower constellation set theory. Part I: Compatibility and phasing," *IEEE Transactions onAerospace and Electronic Systems*, Vol. 44, No. 3, 2008, pp. 953–962.

[58] M. P. Wilkins and D. Mortari, "Flower constellation set theory part II: secondary paths and equivalency," *IEEE Transactions on Aerospace and Electronic Systems*, Vol. 44, No. 3, 2008, pp. 964–976.

[59] J. E. Draim, "Lightsat constellation designs," *AIAA Satellite Communications Conference, Washington DC*, 1992, pp. 1361–1369, DOI: 10.2514/6.1992-1988.

[60] J. L. Worthy III, M. J. Holzinger, and K. Fujimoto, "Optical Sensor Constraints on Space Object Detection and Admissible Regions," *AAS/AIAA Astrodynamics Specialist Conference, Hilton Head, SC*, 2013.

[61] R. D. Coder and M. J. Holzinger, "Multi-Objective Design of Optical Systems for Space Situational Awareness," *Preprint submitted to Acta Astronautica*, 2015.

[62] M. J. Holzinger, K. T. Alfriend, C. J. Wetterer, K. K. Luu, C. Sabol, and K. Hamada, "Photometric Attitude Estimation for Agile Space Objects with Shape Uncertainty," *Journal of Guidance, Control, and Dynamics*, Vol. 37, No. 3, 2014, DOI: 10.2514/1.58002.

[63] A. Milani, G. F. Gronchi, M. D. Vitturi, and Z. Knezevic, "Orbit determination with very short arcs. I admissible regions," *Celestial Mechanics and Dynamical Astronomy*, Vol. 90, No. 1-2, 2004, pp. 57–85, DOI: 10.1007/s10569-004-6593-5.

[64] E. G. Stansbery, M. J. Matney, P. H. Krisko, P. D. Anz-Meador, M. F. Horstman, J. N. Opiela, E. Hillary, N. M. Hill, R. L. Kelley, A. B. Vavrin, *et al.*, "NASA Orbital Debris Engineering Model ORDEM 3.0-Users Guide," tech. rep., NASA Johnson Space Center, Houston, TX, 2012.

[65] P. Bonami, M. Kilinc, and J. Linderoth, "Algorithms and software for convex mixed integer nonlinear programs," *Mixed integer nonlinear programming* (J. Lee and S. Leyffer, eds.), Vol. 154, pp. 1–40, Springer Science & Business Media, 2011, DOI: 10.1007/978-1-4614-1927-3 _1.

[66] T. Schildknecht, *Optical Astrometry of Fast Moving Objects Using CCD Detectors*. Zurich, Switzerland: Institut fur Geodasie und Photogrammetrie, 1994.

[67] M. de Feo, A. Graziano, R. Miglioli, and A. Farina, "IMMJPDA versus MHT and Kalman filter with NN correlation: performance comparison," *Radar, Sonar and Navigation, IEE Proceedings*, 1997, pp. 49 – 56, DOI: 10.1049/ip-rsn:19970976.

[68] R. Danchick and G. Newnam, "Reformulating Reid's MHT method with generalised Murty K-best ranked linear assignment algorithm," *IEEE Proceedings - Radar, Sonar and Navigation*, Vol. 153, No. 1, 2006, DOI: 10.1049/ip-rsn:20050041.

[69] J. C. Liou, "Modeling the Large and Small Orbital Debris Populations for Environment Remediation," tech. rep., NASA Orbital Debris Program Office, June 2014.

[70] J. G. Walker, "Some Circular Patterns Providing Continuous Whole Earth Coverage," *Journal of the British Interplanetary Society*, Vol. 24, No. 7, 1971, pp. 369–384.

[71] M. Broder, E. Mahr, D. Barkmeyer, E. Burgess, W. Alvarado, S. Toas, and G. Hogan, "Review of Three Small-Satellite Cost Models," AIAA SPACE Conference and Exposition, Pasadena, CA, 2009.

[72] M. Boghosian and R. Valerdi, "Cost Estimating Methodology for Very Small Satellites," *COCOMO Forum, University of Southern California*, 2011.

[73] E. Mahr and G. Richardson, "Development of the Small Satellite Cost Model (SSCM)," Vol. 8-3832, 2002.

[74] W. J. Larson and J. R. Wertz, "Space Mission Analysis and Design," 3rd edition, Space Technology Library, Microcosm, Appendix, 1999, ISBN: 978-1881883104.

[75] L. Wang, Y. Wang, K. Chen, and H. Zhang, "Optimization of Regional Coverage Reconnaissance Satellite Constellation by NSGA-II Algorithm," 2008, DOI: 10.1109/ICICTA.2008.322.

[76] G. Mavrotas, "Effective implementation of the Epsilon-constraint method in Multi-Objective Mathematical Programming problems," *Applied Mathematics and Computation*, Vol. 213, No. 2, 2009, DOI: 10.1016/j.amc.2009.03.037.

[77] D. E. Goldberg, "Genetic Algorithms in Search, Optimization & Machine Learning," Addison-Wesley, 1989.

APPENDICIES:

A. Orbit Classification

	Radius of Periapsis (km)	Radius of Apoapsis (km)	Inclination (°)
Low Earth Orbit (LEO)	$> R_e$	$< R_e + 2000$	–
LEO: polar	$> R_e$	$< R_e + 2000$	$75 < i < 120$
Medium Earth Orbit (MEO)	$> R_e$	$< 32,000$	–
Geosynchronous Earth Orbit (GEO)	$> 40,000$	$< 45,000$	–
None of the Above (NOTA)	–	–	–

B. Optimization Results

Planes	Satellites	Semimajor Axis (km)	Inclination(°)
1	1	7603	57.6
1	1	7160	56.8
1	1	7124	57.1
1	1	7142	56.9
1	1	7144	56.4
1	1	7675	55.1
1	1	6995	54.4
1	1	7141	55.7
1	1	6997	57.7
1	1	6999	56.7
2	2	7393	54.7
2	2	7474	56.2
2	2	7348	54.9
1	2	7303	57.8
2	2	7250	53.9
2	2	7293	55.9
2	2	7281	54.0
2	2	7161	53.1
2	2	7294	55.4
2	2	7339	57.4
2	4	7066	54.2
2	4	7003	54.9
2	4	7291	57.8
1	4	7138	59.8
2	4	7136	54.7
2	4	7067	53.7
3	4	7004	40.0
2	4	7004	54.7
2	4	7047	54.8
2	4	7134	54.4

Planes	Satellites	Semimajor Axis (km)	Inclination(°)
2	6	7134	52.9
2	6	7128	53.0
2	6	7114	53.2
2	6	7001	51.7
2	6	7116	52.7
2	6	7132	53.9
2	6	7055	54.1
2	6	7134	53.6
2	6	7076	53.1
2	6	7331	52.5
2	8	7362	62.3
2	8	7338	61.4
2	8	7239	60.0
2	8	7307	68.7
2	8	7357	62.7
2	8	7262	61.0
2	8	7186	54.6
2	8	7197	52.5
2	8	7329	58.2
2	8	7316	68.6
6	12	6995	45.1
6	12	7375	41.7
2	12	7377	50.9
2	12	7440	49.5
5	12	7465	43.8
4	12	7357	30.0
4	12	7346	31.8
4	12	7277	33.3
4	12	7299	32.6
4	12	7317	32.4
3	18	7224	30.7
2	18	7335	35.9
6	18	7362	28.3
3	18	7236	28.4
3	18	7136	28.8
5	18	7264	28.0
6	18	7173	30.5
5	18	7215	29.6
5	18	7354	29.3
6	18	7303	31.3

Planes	Satellites	Semimajor Axis (km)	Inclination(°)
8	24	7258	28.6
3	24	7305	30.5
8	24	7445	28.7
3	24	7456	27.8
3	24	7268	28.4
8	24	7324	27.3
8	24	7345	28.7
3	24	7356	27.8
3	24	7368	28.4
8	24	7345	28.7
13	36	7453	27.8
9	36	7328	27.7
9	36	7312	28.5
8	36	7358	27.3
13	36	7319	27.5
13	36	7460	27.8
13	36	7361	27.3
6	36	7342	32.2
6	36	7542	33.2
13	36	7419	27.5